Key Points:
- The estimated PBLH is sensitive to the critical Ri_b and surface friction effect in the computation with the Ri_b method
- The diurnal climatology of PBLH revealed by AMDAR profiles exhibits expected seasonal and spatial variations
- The ERA5 reanalysis product overestimates the daytime PBLH and fails to capture its peak time

Supporting Information:
- Supporting Information S1

Correspondence to:
K. Sun,
kangsun@buffalo.edu

Diurnal Climatology of Planetary Boundary Layer Height Over the Contiguous United States Derived From AMDAR and Reanalysis Data

Yuanjie Zhang[1], Kang Sun[2] , Zhiqiu Gao[1,3] , Zaitao Pan[4] , Michael A. Shook[5] , and Dan Li[6]

[1]School of Atmospheric Physics, Nanjing University of Information Science and Technology, Nanjing, China, [2]Department of Civil, Structural and Environmental Engineering and Research and Education in Energy, Environment and Water Institute, University at Buffalo, Buffalo, NY, USA, [3]State Key Laboratory of Atmospheric Boundary Layer Physics and Atmospheric Chemistry, Institute of Atmospheric Physics, Chinese Academy of Sciences, Beijing, China, [4]Department of Earth and Atmospheric Sciences, Saint Louis University, St. Louis, MO, USA, [5]NASA Langley Research Center, Hampton, VA, USA, [6]Department of Earth and Environment, Boston University, Boston, MA, USA

Abstract The diurnal variation of the planetary boundary layer height (PBLH) over the contiguous United States (CONUS) is examined using Aircraft Meteorological Data Reports (AMDAR) at 54 major airports and the ERA5 reanalysis product. The bulk Richardson number method is used to derive the PBLH at hourly scales from the AMDAR profiles. It is found that the estimated PBLH is sensitive to the value of the critical bulk Richardson number and to the consideration of the surface friction effect, especially under stable and near-neutral conditions. Parameters constrained by field campaign observations are finally selected to estimate the PBLH. The results reveal that the diurnal climatology of PBLH exhibits seasonal and spatial variations, with greater diurnal variations in spring and summer and in the western regions. It is demonstrated that the traditional twice-daily radiosonde data may roughly capture the diurnal amplitude of PBLH in the western but not the eastern CONUS. Compared to the AMDAR data, the ERA5 reanalysis product overestimates the daytime PBLH throughout the CONUS by 18–41% and shows an earlier peak time by 1–2 hr in the western regions and a later peak time by 1 hr in the eastern regions.

1. Introduction

The planetary boundary layer (PBL) is the lowest part of the atmosphere, directly influenced by the Earth's surface, and the link between the surface and the free atmosphere above the PBL (Garratt, 1992; Stull, 1988). The height of the top of the PBL (PBLH) is a key parameter that determines the vertical extent of turbulent mixing, which is critical to many environmental and climate issues such as the vertical distribution of air pollutants and the formation of fog and cloud (Cohen et al., 2011; Cohen & Prinn, 2011; Liu & Liang, 2010; Su et al., 2018). The PBLH varies significantly in response to surface heating and cooling in a typical diurnal cycle. The PBL is often shallow (<500 m) at night due to the strong thermal inversion resulting from radiative cooling. It grows deep (1–3 km) in the daytime when solar radiation heats the surface and generates convective turbulence. However, it is a significant challenge to directly observe atmospheric turbulence, and hence the PBLH is often diagnosed from measurements of mean vertical profiles of temperature, humidity, and wind (Seibert, 2000; Seidel et al., 2010).

Mean vertical profiles of temperature, humidity, and wind are routinely measured by radiosondes globally, but these radiosondes are typically launched only at 00 and 12 UTC, which, over the contiguous United States (CONUS), roughly correspond to early morning and late afternoon. More frequent soundings (e.g., four to eight times a day) can be obtained through intensive field campaigns (e.g., Angevine et al., 2012; Blaskovic et al., 1991; Liu & Liang, 2010), but field campaigns are inherently limited to short periods and certain locations. Hence, previous investigations on the PBLH using radiosonde data either did not resolve the full diurnal cycle or were limited to certain periods and locations (Guo et al., 2016; Liu & Liang, 2010; Seidel et al., 2012). For example, Holzworth (1964) studied the PBLH climatology in terms of the monthly mean maximum mixing depth over the CONUS based on radiosonde data from 45 stations. However, these monthly mean maximum mixing depth values were simply estimated by extending a dry adiabatic lapse rate from the maximum surface temperature to its intersection with the monthly averaged temperature profile

from 03 UTC radiosonde observations. Using radiosonde observations (two to eight times a day) from 14 field campaigns around the world, Liu and Liang (2010) investigated the diurnal variation of PBLH, which sheds important insights into the PBLH behavior at diurnal scales. Seidel et al. (2012) studied the seasonal variation of PBLH at 00 and 12 UTC with radiosonde observations and the diurnal variation of PBLH with a reanalysis product (3-hourly) and two climate models (6-hourly) over the CONUS and Europe. Guo et al. (2016) compiled a PBLH climatology over China using radiosonde data collected by the China Radiosonde Network (again mostly at 00 and 12 UTC but with certain intensive observing periods in summer featuring four soundings a day). With this data set, the PBL characteristics under different stability conditions and the long-term trends of PBLH over different geographic regions in China were further explored (Guo et al., 2019; Zhang et al., 2018).

In addition to traditional radiosonde data, the PBLH can be also estimated from various other data sources, such as ground-based ceilometer (Eresmaa et al., 2006; van der Kamp & McKendry, 2010), lidar (Hennemuth & Lammert, 2006; Sawyer & Li, 2013; Tucker et al., 2009), and wind-profiling and weather radar (Angevine et al., 1994; Bianco & Wilczak, 2002; Lange et al., 2015). These data provide high-vertical resolution profiling of the lower troposphere but are limited to point scale and often short-duration periods. Satellite remote sensing platforms provide another alternative with improved spatial coverage (Guo et al., 2011; Jordan et al., 2010; McGrath-Spangler & Denning, 2012; Ratnam & Basha, 2010), but the accuracy in the estimated PBLH from satellite data is relatively low, and extensive ground-based validation is needed (Chahine et al., 2006; Su et al., 2017; Zhang et al., 2016). In addition, satellite observations typically do not resolve the diurnal cycle of the PBL due to the temporal revisit frequency (e.g., ~16 days for the Cloud-Aerosol Lidar and Infrared Pathfinder Satellite Observation or CALIPSO mission).

The other data source that provides routine observations of the PBL is the Aircraft Meteorological Data Reports (AMDAR) data, which are automated weather logs from commercial aircraft globally (Moninger et al., 2003). Compared to radiosonde data, the AMDAR program provides vertical profiles (through ascents and descents made at airports) at considerably higher temporal resolutions that captures the diurnal variation of the PBLH. Comparisons between AMDAR and collocated radiosonde data revealed that temperature, humidity, and wind in AMDAR ascent/descent profiles agree well with radiosonde soundings (Petersen et al., 2016; Schwartz & Benjamin, 1995; Zhang et al., 2019). The AMDAR data have been widely used to improve short-term forecasts in numerical weather prediction (Cardinali et al., 2003; Moninger et al., 2003; Petersen, 2016; Petersen et al., 2016; Zhu et al., 2015), but their use for studying the PBL is sparse. Rahn and Mitchell (2016) examined the diurnal variations of PBL temperature profiles and the estimated PBLH using temperature and wind profiles at three airports in Southern California. More recently, Zhang et al. (2019) developed a decade-long (from 2007 to 2016) data record of hourly PBL profiles of temperature, wind, and humidity with a vertical resolution of 20 m based on AMDAR data over 54 main U.S. airports. They found that this data record is particularly suited for investigating the diurnal variation of the PBL due to their higher temporal resolution in comparison with radiosonde data (Zhang et al., 2019, 2020).

The overarching goal of this work is to derive a diurnal climatology of PBLH over the CONUS using the AMDAR data. To do so, we first estimate the PBLH from the hourly profiles generated by Zhang et al. (2019) and validate the estimated PBLH with independent field measurements. Then we examine the geographic and seasonal variabilities of the PBLH diurnal climatology and compare the results with a high-resolution reanalysis product. Built upon previous work on AMDAR profiles, this paper presents a more complete analysis of the diurnal variation of PBLH over the CONUS and compares the diurnal climatology of PBLH estimated from AMDAR data to a reanalysis product, which has not been attempted before.

2. Data

2.1. Hourly PBL Profiles From AMDAR

The AMDAR program was established by the World Meteorological Organization (WMO) and has grown rapidly over the past few years, including about 5,000 aircraft worldwide that contribute more than 600,000 temperature and wind observations per day, 450,000 of which are over the CONUS (Petersen, 2016). The AMDAR data include coordinates (time, latitude, longitude, and pressure altitude) and measurements of air temperature, wind components, and, to a lesser extent, specific humidity. The AMDAR data are publically available on the Meteorological Assimilation Data Ingest System web service portal (https://madis-
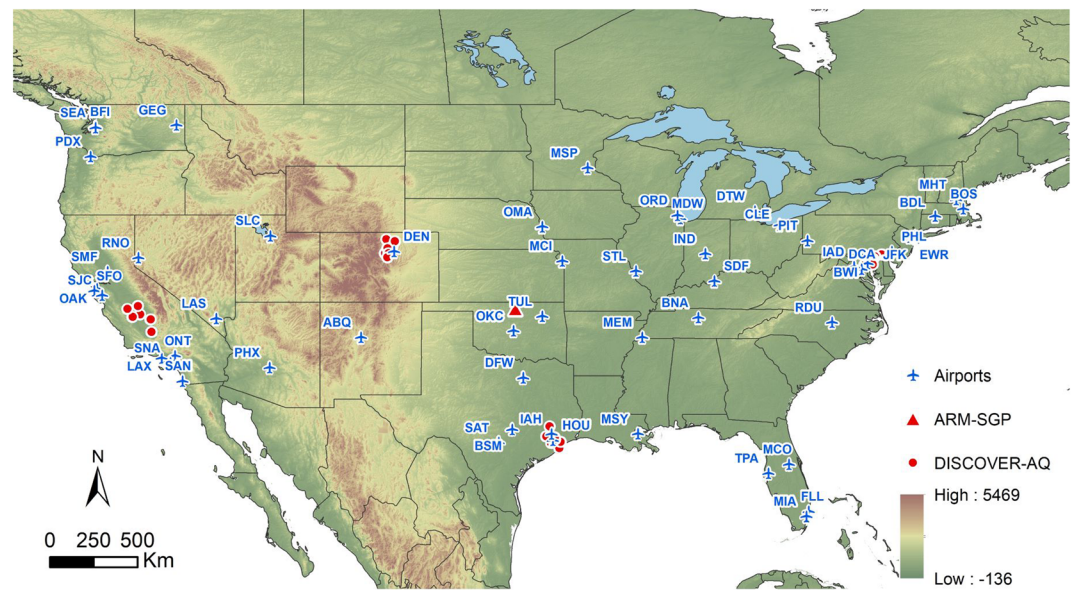
Figure 1. Locations of the selected airports and field campaigns. The digital elevation model (DEM) is from the Global Land One-km Base Elevation Project (GLOBE; Hastings et al., 1999).

data.cprk.ncep.noaa.gov/madisPublic1/data/archive/). Hence, these data have gone through preliminary data quality control and have data quality indicators associated with them. Data points that failed the level I data quality control are excluded in our study.

Since the amount of AMDAR data varies across airports, we select 54 airports (shown in Figure 1) with AMDAR data in at least 20% of the hours in each year during 2007–2016. These airports are mainly located in the northeast, along the west coast, and in the central United States, but they cover a broad range of climatic regimes. In a previous study (Zhang et al., 2019), we developed a consistent data set of hourly PBL profiles over these 54 airports by merging all ascent and descent soundings within 1 hr and interpolating them onto a regular vertical grid with 20-m intervals (see examples in Figure 2). We also compared our derived AMDAR profiles to nearby radiosonde data at 00 and 12 UTC and found good agreement between the two data sources for air temperature, specific humidity, and wind components (Zhang et al., 2019). In this study, we derive PBLH from these hourly profiles.

2.2. Reanalysis Data

In this study, we use a high-resolution reanalysis product (ERA5) generated by the European Centre for Medium-Range Weather Forecasts (ECMWF). We choose ERA5 as it is the only reanalysis product that provides hourly data, which is consistent with the temporal resolution of the processed AMDAR profiles. The ERA5 data are available in the Climate Data Store (https://cds.climate.copernicus.eu/) on regular latitude-longitude grids at 0.25° × 0.25° resolution, with atmospheric parameters on 37 pressure levels. In this study, we only use the PBLH and surface friction velocity from ERA5.

2.3. PBLH From Field Campaigns
2.3.1. NASA DISCOVER-AQ Campaigns

To validate our estimates of PBLH, we use the PBLH derived from in situ aircraft spiral profiles made at the NASA DISCOVER-AQ campaigns, which include four phases: Maryland-DC in July 2011, California in January–February 2013, Texas in September 2013, and Colorado in July–August 2014. In DISCOVER-AQ, the PBL and lower free troposphere were systematically sampled by the NASA P-3B aircraft above a small number of sites by spiral profiling, indicated as red dots in Figure 1. A large collection of vertical profiles was obtained, covering most of the daytime (generally from 2 to 10 hr after sunrise). The spirals are about 5 km in diameter, extending from the lower free atmosphere (3–5 km above the surface) to as low as 30 m above the surface. For each spiral, the PBLH was identified manually based on sharp gradients of potential temperature, relative humidity, water vapor, carbon dioxide, and other important tracers such as nitrogen dioxide and aerosol extinction (see Figures S1–S3 and text in the supporting information for details). The
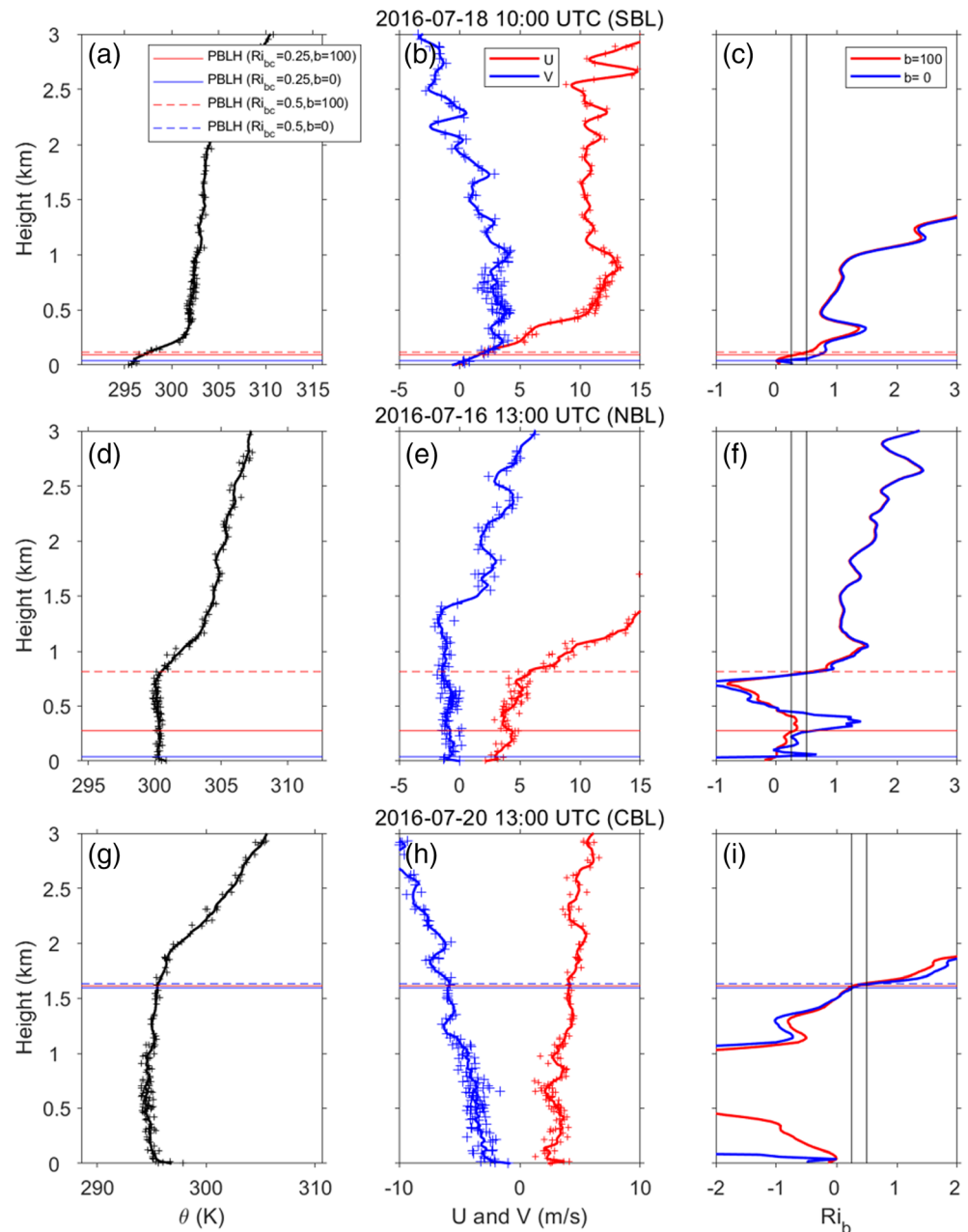
Figure 2. Vertical profiles of (left) potential temperature, (middle) wind components, and (right) the bulk Richardson number at (a–c) 10 UTC 18 July 2016, (d–f) 13 UTC 16 July 2016, and (g–i) 13 UTC 20 July 2016 at the Boston Logan International Airport. The PBL at the three times are identified as SBL, NBL, and CBL, respectively. For profiles of temperature and wind, plus signs indicate raw AMDAR observational points while bold lines indicate the interpolated AMDAR profiles (Zhang et al., 2019). Horizontal lines indicate the PBLH computed from the interpolated AMDAR profiles using the bulk Richardson number method with different critical bulk Richardson numbers (0.25 and 0.5, indicated by the vertical lines in c, f, and i) and b values (0 and 100).

PBLHs were identified from 218 out of 253 spirals at Maryland-DC (MD), 176 out of 195 spirals at Texas (TX), and 202 out of 220 spirals at Colorado (CO). The DISCOVER-AQ California phase was not included because all spirals were located in the San Joaquin Valley with no airport in our selected AMDAR data (see Figure 1).

2.3.2. Atmospheric Radiation Measurement Experiment at the Southern Great Plains Site

Atmospheric soundings were launched at high frequency (usually four soundings a day at 0530, 1130, 1730, 2330 UTC) during the Atmospheric Radiation Measurement (ARM) experiment at the Southern Great Plains

site (referred to as ARM-SGP hereafter, 36.61°N, 97.49°W), indicated as the red triangle in Figure 1. To match the time span of the AMDAR data analyzed in this study, we use soundings from 2007 to 2016. We derive PBLH from these soundings using the same method as deriving PBLH from AMDAR data (to be elaborated in section 3) and compare the estimated PBLH at ARM-SGP to the AMDAR-based PBLH at Will Rogers World Airport (OKC, 35.4°N, 97.6°W), which is the nearest airport to ARM-SGP.

3. Determination of PBLH Using the Bulk Richardson Number Method

3.1. Definition

Many methods have been proposed to diagnose the PBLH (Seibert, 2000), including identification of critical gradient, maximum/minimum, or discontinuity in temperature, wind, and/or humidity profiles. However, the distinct features required by these methods are often ambiguous or even not present (Zhang et al., 2014). As such, manual inspection is often conducted in experimental studies where data volume is small (e.g., DISCOVER-AQ). Given the large number of profiles in the AMDAR archive, an automated method suitable for a variety of atmospheric stability conditions (stable, near-neutral, and convective) is needed. The bulk Richardson number (Ri_b) method has been proven to be a reliable method for computing the PBLH (Seidel et al., 2012) and thus is adopted in our study. We note that the PBLH from ERA5 is also computed using the Ri_b method on both land and water (ECMWF, 2017).

The Ri_b is defined as the ratio of buoyancy destruction and shear production of turbulence, expressed as

$$Ri_b = \frac{(g/\theta_{vs})(\theta_{vz} - \theta_{vs})(z - z_s)}{(u_z - u_s)^2 + (v_z - v_s)^2 + bu_*^2},$$

(1)

where z_s is the height of the lower boundary for the PBL, often taken as 20 or 40 m (Vogelezang & Holtslag, 1996). θ_{vs} and θ_{vz} are the virtual potential temperatures at height z_s and z, respectively, g/θ_{vs} is the buoyancy parameter, u and v are component wind speeds, b is an empirical coefficient, and u_* is the surface friction velocity. The Ri_b method assumes that the PBLH is the height at which the Ri_b reaches a threshold value (the critical bulk Richardson number, Ri_{bc}). At present, the most widely used Ri_{bc} values are 0.25 (e.g., Hong, 2010) and 0.5 (e.g., Holtslag & Boville, 1993). The PBLH from ERA5 is identified using the Ri_b method with a critical value of 0.25.

Because of the scarcity of humidity measurements in the AMDAR archive, in this study, we use potential temperature as a surrogate to virtual potential temperature in Equation 1. It should be noted that neglecting the contribution of humidity to the buoyancy effects may affect the estimated PBLH over coastal areas. The bu_*^2 term, which represents the mechanical production of turbulence due to surface friction, makes the Ri_b method more applicable for the near-neutral condition (Seibert, 2000). A value of 100 was suggested for b by Vogelezang and Holtslag (1996). We also test $b = 0$ to evaluate the impact of ignoring the surface friction effect. We note that the PBLH from ERA5 is diagnosed with $b = 0$. In this study, the surface friction velocity (u_*) data are from the ERA5 data at the nearest grid to the airport, since they are not available from the AMDAR data. However, the surface friction velocity from the ERA5 data is representative for a whole grid cell, which may not represent the conditions near the airport, so we have also tested simple constant values for u_*.

3.2. Sensitivity Analysis

Figure 2 shows three typical AMDAR profiles under stable, near-neutral, and convective PBL conditions at the Boston Logan International Airport (BOS), as well as the PBLHs computed by the Ri_b method with different Ri_{bc} and b values. The AMDAR profiles are classified according to the atmospheric stability by calculating the near-surface potential temperature differences between the 200 and 50 m heights (PTD$_{200-50}$) and between the 100 m height and surface (PTD$_{100-surf}$), roughly following Liu and Liang (2010). Therefore, in the classification of PBL types, AMDAR profiles are first interpolated to the vertical resolution of 50 m (the PBLH computation is based on AMDAR profiles at the original vertical resolution of 20 m). Specifically, if the PTD$_{200-50}$ > 0.1 K and PTD$_{100-surf}$ > 0 K, the PBL is identified as a stable boundary layer (SBL); if the PTD$_{200-50}$ < −0.1 K, the PBL is identified as a convective boundary layer (CBL); and other cases can be considered as near-neutral boundary layers (NBLs).
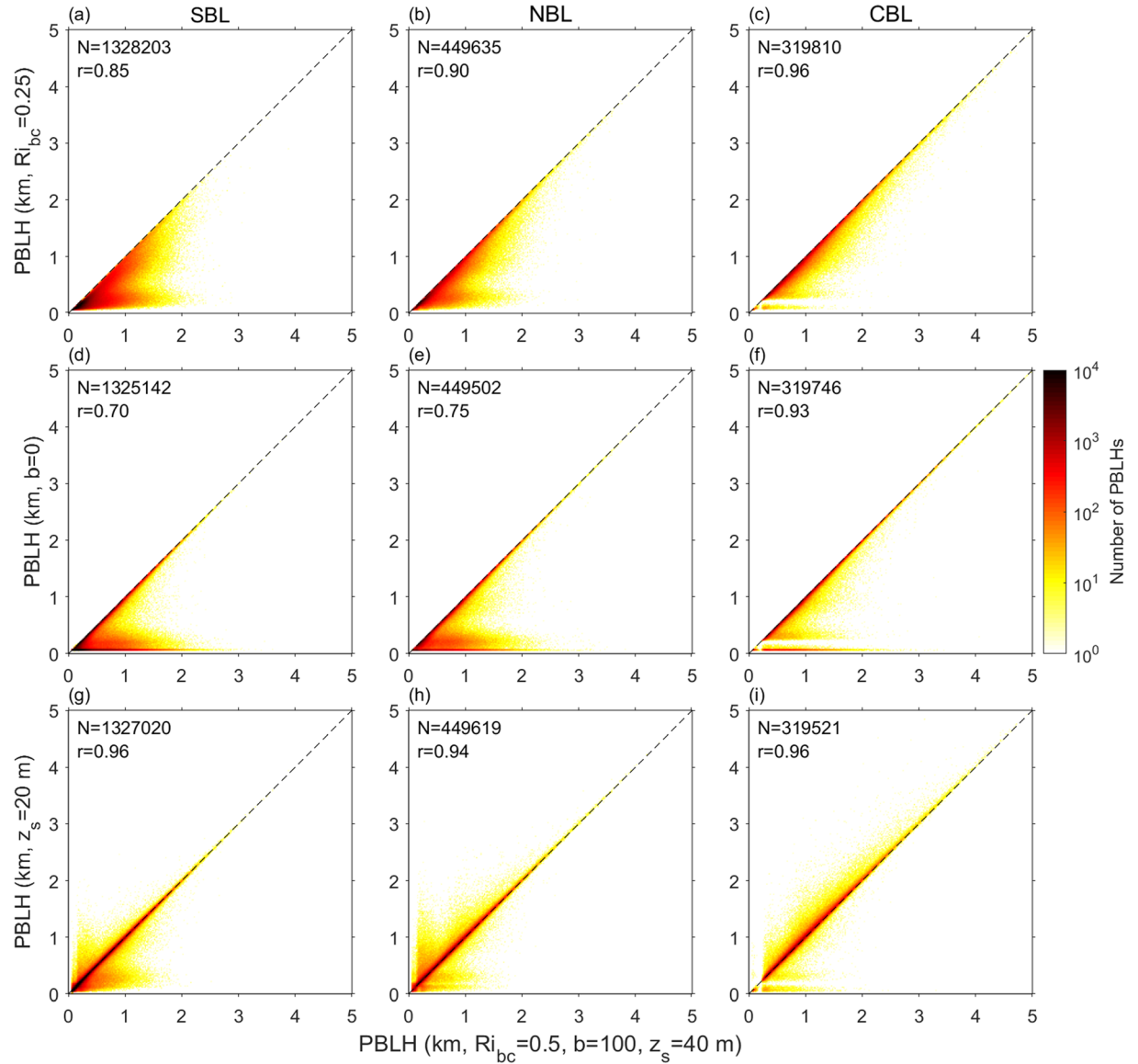
Figure 3. Comparisons of the PBLHs computed using the Ri_b method with (a–c) $Ri_{bc} = 0.25$ and $Ri_{bc} = 0.5$, (d–f) $b = 0$ and $b = 100$, and (g–i) $z_s = 20$ m and $z_s = 40$ m. N indicates the number of valid PBLHs over 54 airports during 2007–2016. Results of PBLHs from SBL, NBL, and CBL are shown in the left, middle, and right panels, respectively.

It can be seen that different Ri_{bc} values (0.25 or 0.5) do not affect much the computed PBLHs for the SBL and CBL examples but yield very different PBLHs for the NBL example due to the large variation of Ri_b near the surface. The consideration of surface friction effect or not (i.e., $b = 100$ or $b = 0$) has an important impact on the resultant PBLH in stable and near-neutral conditions. For example, in the NBL case, the computed PBLH with $Ri_{bc} = 0.5$ is 837 m when considering the surface friction effect ($b = 100$), while only 40 m if the surface friction effect is ignored ($b = 0$). This highlights the importance of considering the surface friction effect in the near-neutral condition (Seibert, 2000; Vogelezang & Holtslag, 1996).

To rigorously quantify the sensitivity of the estimated PBLHs to the parameters used in the Ri_b method, scatter plots are made to compare PBLH estimation under SBL, NBL, and CBL conditions using different Ri_{bc} (0.25 and 0.5), b (0 and 100), and z_s (20 and 40 m) values (Figure 3). As can be seen from the first two rows (panels a–f), the PBLHs computed with $Ri_{bc} = 0.5$ or $b = 100$ are systematically larger than those computed with $Ri_{bc} = 0.25$ or $b = 0$. It suggests that the Ri_{bc} value and the inclusion of the surface friction effect have

Table 1
Correlation Coefficients Between PBLHs From DISCOVER-AQ and ARM-SGP and PBLHs Estimated From AMDAR Data

Parameter sets	AMDAR (DEN) vs. DISCOVER-AQ (CO)	AMDAR (BWI) vs. DISCOVER-AQ (MD)	AMDAR (HOU) vs. DISCOVER-AQ (TX)	AMDAR (OKC) vs. ARM-SGP
$Ri_{bc} = 0.25$, $b = 100$, $z_s = 20$ m	0.44	0.50	0.56	0.63
$Ri_{bc} = 0.25$, $b = 100$ $z_s = 40$ m	0.46	0.42	0.58	0.65
$Ri_{bc} = 0.25$, $b = 0$, $z_s = 20$ m	0.44	0.48	0.51	0.49
$Ri_{bc} = 0.25$, $b = 0$, $z_s = 40$ m	0.40	0.32	0.45	0.44
$Ri_{bc} = 0.50$, $b = 100$, $z_s = 20$ m	**0.50**	**0.51**	0.61	0.67
$Ri_{bc} = 0.50$, $b = 100$, $z_s = 40$ m	0.49	0.48	**0.62**	**0.70**
$Ri_{bc} = 0.50$, $b = 0$, $z_s = 20$ m	0.43	0.47	0.59	0.52
$Ri_{bc} = 0.50$, $b = 0$, $z_s = 40$ m	0.40	0.38	0.49	0.48

Note. All correlation coefficients are statistically significant ($p < 0.05$). The optimal set of parameters is presented in bold.

significant impacts on the estimated PBLH, especially for SBL and NBL. Excluding the surface friction effect ($b = 0$) often leads to unrealistically low PBLH under stable and near-neutral conditions (Figures 3d and 3e). In contrast, the PBLHs based on different z_s values (20 and 40 m; Figures 3g–3i) are highly correlated with each other and do not seem to show any consistent differences.

3.3. Validation Against Field Campaign Observations

According to the above analysis, the Ri_{bc} and b values have significant impacts on the estimated PBLHs when using the Ri_b method. To obtain the optimal parameters (Ri_{bc}, b, and z_s), we test eight different parameter sets by comparing the estimated PBLHs to the PBLHs derived from DISCOVER-AQ spiral profiles and ARM-SGP soundings. The PBLHs from DISCOVER-AQ profiles are manually determined and thus completely independent from AMDAR, whereas the same Ri_b method with the same set of parameters is applied to derive PBLH from ARM-SGP. The results in terms of correlation coefficients are presented in Table 1. The significantly improved correlation coefficients with $b = 100$ relative to $b = 0$ demonstrate that the surface friction term is necessary in the PBLH computation with the Ri_b method. The parameter sets of $Ri_{bc} = 0.5$, $b = 100$, and $z_s = 20$ and 40 m yield higher correlation coefficients between the AMDAR PBLHs and the validation data sets. Considering that there are no systematical biases between PBLHs estimated by different z_s values (20 and 40 m; Figures 3g–3i), the parameter set of $Ri_{bc} = 0.5$, $b = 100$, and $z_s = 40$ m is selected for the following analysis, since a larger z_s value helps avoid the influence of underlying surfaces on the lowest data points of the AMDAR profiles. We also test the gradient Ri method (e.g., Seibert, 2000; Zilitinkevich & Baklanov, 2002) and the potential temperature gradient method (e.g., Dai et al., 2011; Marsik et al., 1995). The results of those two methods are both worse than that of the Ri_b method (not shown).

Figures 4a–4c show comparisons of the estimated PBLHs at Denver International Airport (DEN), Baltimore/Washington International Thurgood Marshall Airport (BWI), and William P. Hobby Airport (HOU) using the selected parameter set (i.e., $Ri_{bc} = 0.5$, $b = 100$, and $z_s = 40$ m) and the PBLHs from DISCOVER-AQ data at CO, MD, and TX. For DISCOVER-AQ PBLHs, only spiral sites within 50 km from the AMDAR airport are used in the comparison. The AMDAR PBLHs computed with the Ri_b method agree well with the DISCOVER-AQ PBLHs for CBL, while show significant underestimations for most SBL samples and part of NBL samples, with overall correlation coefficients of 0.49, 0.48, and 0.62 at CO, MD, and TX, respectively. The dot size in Figures 4a–4c indicates the distance between the DISCOVER-AQ spiral central coordinates and the corresponding airport in AMDAR data. In general, there is a better agreement when the DISCOVER-AQ spirals and AMDAR airports are close, especially at TX where the bay breeze may introduce significant spatial heterogeneity (Darby, 2005). This is also consistent with our previous work showing that there is a better agreement between AMDAR and radiosonde data as their separation becomes smaller (Zhang et al., 2019).

To explore the underestimation of AMDAR PBLHs for SBL and NBL, we also test AMDAR PBLHs derived using a fixed value (0.3 m/s) for u_*, which is larger than the median value of u_* (0.2 m/s) in ERA5 (Figure S4). The results show better agreement between the diagnosed AMDAR PBLHs and the field campaign observations, with correlation coefficients of 0.65 and 0.57 at CO and MD, respectively (Figure S5). This implies that
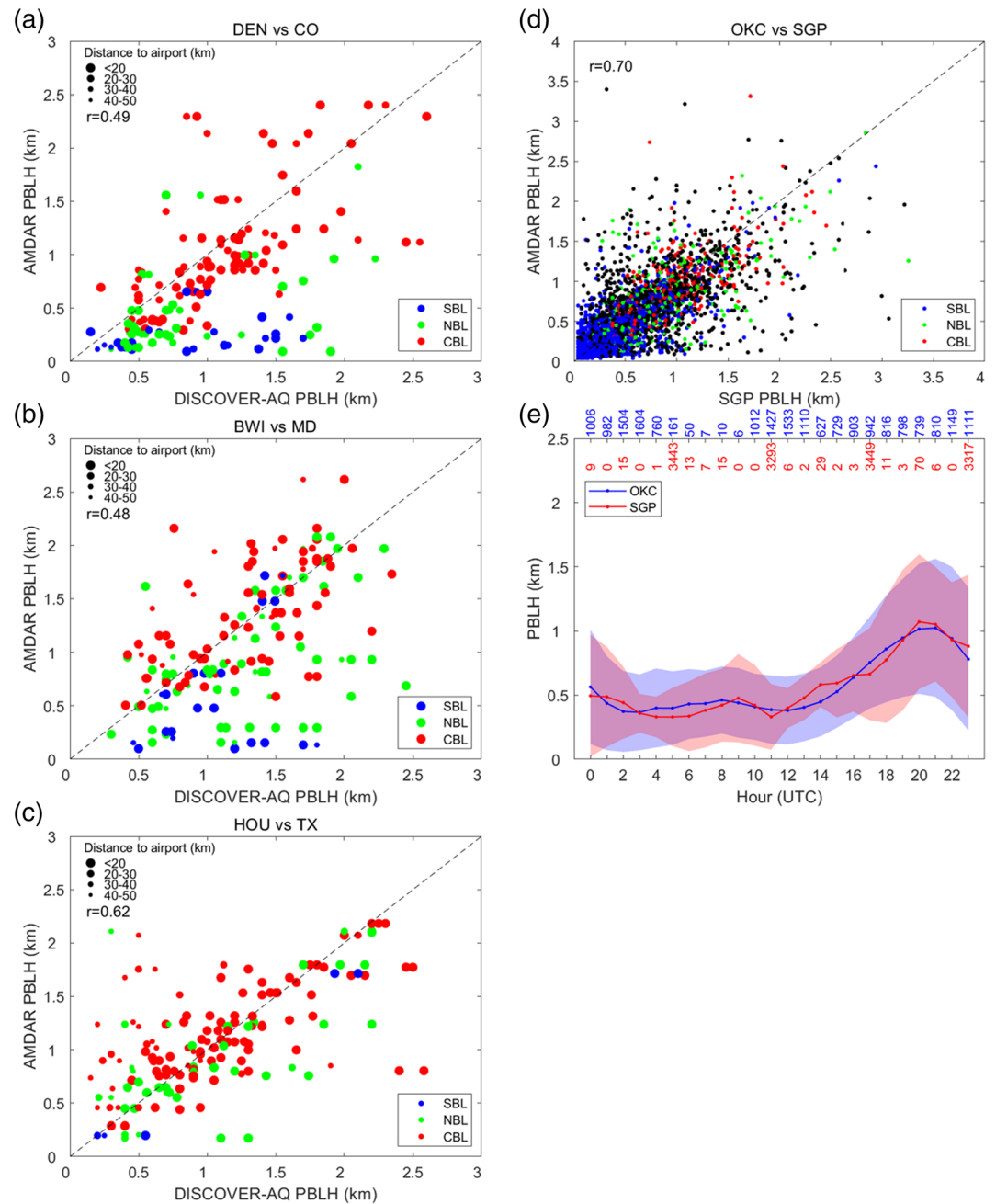
Figure 4. Comparisons of PBLHs derived from AMDAR data to PBLHs from DISCOVER-AQ data at (a) CO, (b) MD, (c) TX, and from (d–e) ARM-SGP data. In (a–c), the dot size indicates the distance between the DISCOVER-AQ spiral central coordinates and the corresponding airport in AMDAR data. In (a–d), PBLHs from SBL, NBL, and CBL are indicated by blue, green, and red dots, respectively. In (e), the solid lines show the mean diurnal cycles of PBLH at OKC (blue) and ARM-SGP (red) from 2007 to 2016 and the shade indicate the standard deviation. The numbers at the top indicate the number of profiles included in each hourly bin.

u_* from ERA5 may underestimate the local surface stress near the airport and more accurate u_* data may further improve the PBLH determination. However, in this paper, we use u_* from ERA5, which seems more justified especially considering that we will compare the AMDAR and ERA5 PBLHs.

The estimated PBLHs at OKC and those estimated from soundings at ARM-SGP are compared in Figure 4d. The scatter plot shows good agreement between AMDAR and ARM-SGP PBLHs, with a correlation
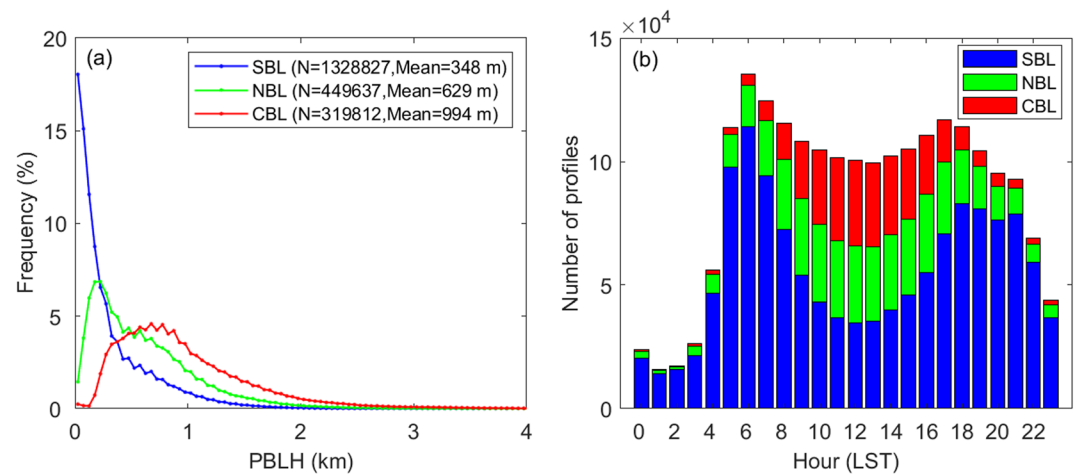
Figure 5. (a) Frequency distributions of AMDAR PBLH in stable, near-neutral, and convective boundary layers over CONUS from 2007 to 2016. N indicates the number of samples. The mean PBLHs of different stability regimes are also shown. (b) The total number of AMDAR profiles at each local hour. The numbers of AMDAR profiles in stable, near-neutral, and convective conditions are shown in blue, green, and red, respectively.

coefficient of 0.7, even though the distance between the two data sources is larger than 100 km. The composite diurnal PBLH variations at OKC and SGP are shown in Figure 4e. Note that ARM-SGP soundings are mainly collected at 05, 11, 17, and 23 UTC, while AMDAR profiles are rare at 07, 08, and 09 UTC due to the lack of air traffic around midnight, as shown by the numbers at the top of Figure 4e. As a result, all lines in Figure 4e have been smoothed using a 3-hr window. The diurnal variations of AMDAR and ARM-SGP PBLHs also agree reasonably well in terms of mean and variability (Figure 4e). One should note that the PBLHs from AMDAR at OKC airport and from ARM-SGP are calculated using the same method and the same set of parameters, although the observation modes are very different (commercial airline logs vs. balloon-born soundings). The relatively high PBLH during nighttime (around 500 m) may result from the nocturnal low-level jet over the area, and we caution that the uncertainty is large (see the standard deviation). In summary, these comparisons with field campaign observations give us confidence that the AMDAR data can be used to analyze the diurnal climatology of PBLH over the CONUS.

4. Results

This section presents the diurnal climatology of PBLH from the AMDAR data, including basic statistics, diurnal/seasonal variations, and spatial variations across the CONUS. Comparisons between the PBLH diurnal profiles from AMDAR and ERA5 are also conducted to assess the performance of ERA5 PBLH product over different regions in the CONUS and in different seasons.

4.1. AMDAR PBLH Diurnal Climatology Averaged Over the CONUS

Figure 5a presents the frequency distributions of AMDAR PBLH under stable, near-neutral, and convective conditions. The PBLH for SBL is rather narrow, with 94% of the estimated PBLH lower than 1 km and a mean value of 348 m. In contrast, the CBL has a wider PBLH range, with 61% of the estimated PBLH lower than 1 km and a mean value of 994 m. The distribution of PBLH for NBL falls in between, with 83% of the estimated PBLH lower than 1 km and a mean value of 629 m. The PBLH estimates rarely exceed 3 km in general, except in the Southwest over the warm season (see Figure 8).

The occurrences of SBL, NBL, and CBL regimes across the diurnal cycle are illustrated in Figure 5b. The total numbers of available profiles are around 20,000 from 01 to 04 local solar time (LST) and much larger at other times, with two maxima over 110,000 at 06 and 17 LST, respectively. The smaller number of available profiles in the first 4 hr is due to the early morning minimum of commercial air traffic (Moninger et al., 2003). As one can see, the SBL regime occurs during the whole day and dominates at night, while the CBL regime mainly occurs in the daytime, peaking around the noon and declining substantially in the morning and evening.
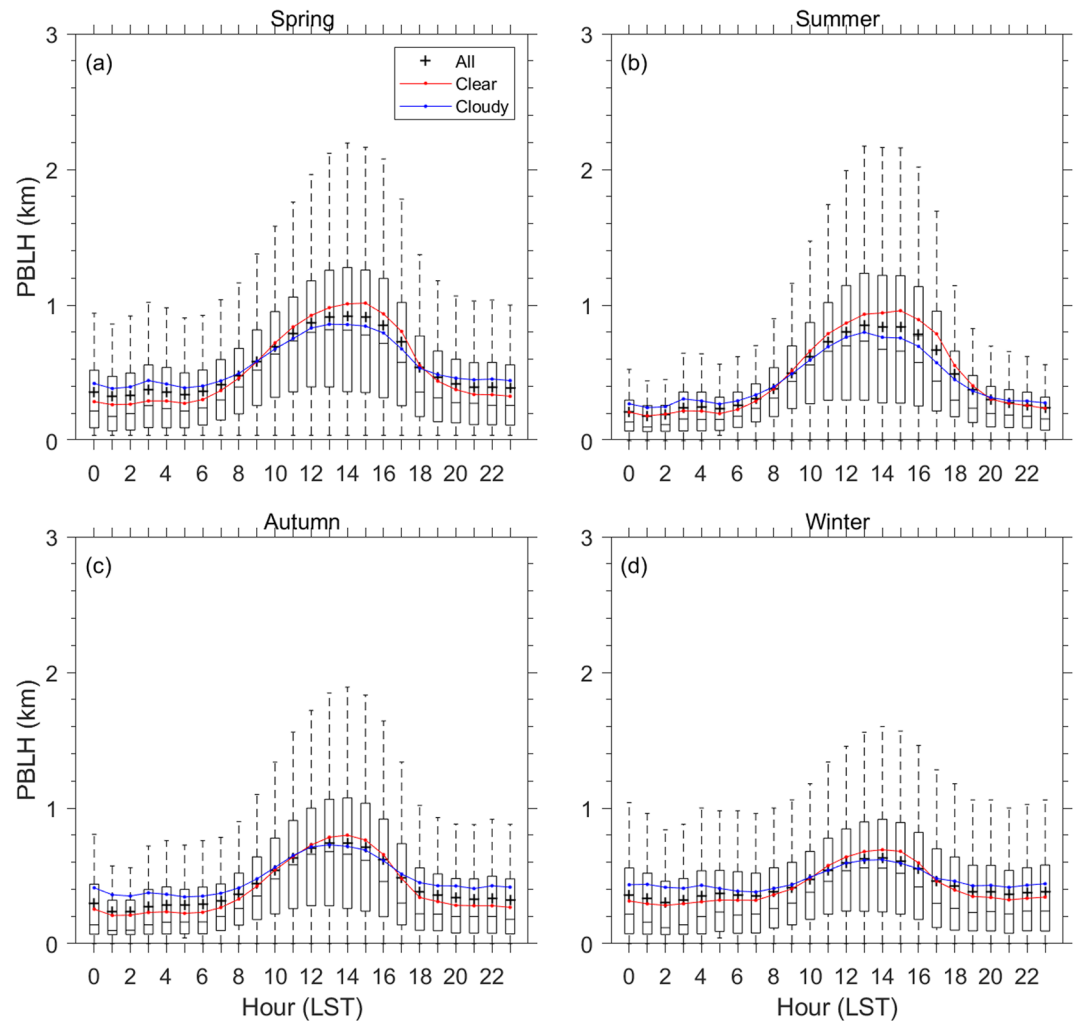
Figure 6. Boxplots of AMDAR PBLH (km) in (a) spring, (b) summer, (c) autumn, and (d) winter during 2007–2016. The horizontal line, the box, and the whiskers represent the median, the interquartile range, and the 5th and 95th percentiles, respectively. The mean PBLH of all profiles is indicated by the black plus signs, while the mean PBLHs under clear and cloudy conditions are shown by the red and blue dotted lines, respectively.

The NBL regime occurs more frequently than CBL at early morning and early evening. This is expected since the near-neutral condition often occurs in the transition between daytime CBL and nocturnal SBL. The frequent occurrence of daytime SBLs seen in Figure 5b is largely driven by the autumn and winter, when daytime SBLs are prevalent due to low surface temperature (Figure S6). Many of the coastal airports have SBLs through the whole diurnal cycle, which could also contribute to the overall prevalence of SBL.

Figure 6 shows the diurnal variations of AMDAR PBLH in each season (spring: March–May, MAM; summer, June–August, JJA; autumn: September–November, SON; winter: December–February, DJF) in terms of the 5th, 25th, 50th, 75th, and 95th percentiles (boxplot) as well as the mean (plus signs). The results reveal well-defined diurnal cycles of PBLH, featuring a distinct peak in the afternoon and a morning (evening) transition around 06 (19) LST. The mean PBLHs are less than 400 m at night in all seasons but can reach over 800 m during daytime in spring and summer with the 95th percentile reaching 2 km at 13–16 LST and over 600 m in autumn and winter. Consistent with the mean values, the variabilities in terms of interquartile ranges are also smaller at night and larger during daytime. The hours of maximum mean and median PBLH are similar among seasons. However, it is interesting to observe that the mean PBLH is generally higher than the median PBLH across the diurnal cycle in all seasons, especially at nighttime.

This indicates that the PBLHs at each hour are not normally distributed but skewed toward higher values (see also in Figure 5a).

Comparing the PBLH in different seasons, it is found that its diurnal variation is stronger in spring and summer and weaker in autumn and winter. During the daytime, the mean and median PBLHs in spring and summer are higher than those in winter (and to a lesser extent those in autumn). This result is consistent with the analysis based on radiosonde data at 00 and 12 UTC by Seidel et al. (2012). In a previous study (Guo et al., 2016), the higher PBLHs in spring and summer in terms of mean and median values were found to be partly associated with the climatologically strong near-surface wind speed in spring and the intense solar radiation in summer, respectively. Note that the daytime variability is also the smallest in winter compared to other seasons.

With cloud cover observations obtained at the airport meteorological stations, available through the Integrated Surface Database (https://www.ncdc.noaa.gov/isd/data-access), the effects of cloud cover on the diurnal evolution of PBLH are also investigated. An hour is classified as clear if it is labeled "Clear" and "Scattered" (oktas do not exceed four) and as cloudy otherwise (Rahn & Mitchell, 2016). Rainy/no-rain hours are not separated due to the complexity of rainfall across seasons and climate zones. During the daytime, the mean PBLH under clear conditions is higher than that under cloudy conditions, because the development of PBL is typically suppressed due to reduced solar radiation and thermal heating at the surface under cloudy conditions. In contrast, thicker boundary layers were formed at nighttime under cloudy conditions, which is likely caused by the less surface radiative cooling when clouds exist. Consequently, the diurnal variation of PBLH is significantly stronger under clear conditions than under cloudy conditions.

4.2. Geographic Variability of AMDAR PBLH

Previous studies have shown that the behavior of PBLH has strong geographic variabilities (Guo et al., 2016, 2019; Seidel et al., 2012). However, how the diurnal climatology of PBLH varies across the CONUS has not been studied using hourly observations given that most previous studies rely on sparse radiosondes (Guo et al., 2016, 2019; Seidel et al., 2012) and/or model data including reanalysis (Konor et al., 2009; Medeiros et al., 2005; Randall et al., 1985; Seidel et al., 2012). Here we fill this research gap by using PBLHs estimated from hourly AMDAR profiles from 2007 to 2016.

To facilitate comparisons between our work and previous studies and also to focus on the spatial variations of key diurnal features, Figures 7–10 present the spatial patterns of mean PBLH at 00 and 12 UTC, diurnal amplitude (maximum and minimum PBLH), and diurnal phase (UTC hours of maximum and minimum PBLHs) in spring, summer, autumn, and winter, respectively. In this subsection, we focus on the AMDAR data which are shown as dots on Figures 7–10, with brief discussions on the comparison between the AMDAR data and the ERA5 data which are shown as the background. Note that in the top panels (subfigures a and b) of Figures 7–10, we examine the mean PBLH to 00 and 12 UTC only to be consistent with traditional radiosonde observational times and previous studies using those radiosonde data. The full diurnal PBLH variations in UTC can be found in Figures S7–S10, and the diurnal PBLH variations in local hours are discussed in sections 4.3 and 4.4. Because the CONUS region spans several time zones, the spatial variations of PBLH observed at a given UTC are complicated by the diurnal variations, as shall be seen later. Note that the mean PBLH at a certain hour is valid only when the total number of AMDAR profiles within the 10-year period (2007–2016) is at least 10. Analyses based on median PBLH are also conducted, which show similar results to those based on mean (not shown).

In spring, as illustrated in Figure 7a, there is a strong east-west gradient for PBLH at 00 UTC, with distinctly higher PBLH in the western United States, which is captured by both AMDAR and ERA5 data. This is because 00 UTC corresponds to late afternoon in the western United States while early evening in the eastern United States, and the PBLH in late afternoon is expected to be higher simply due to the convective conditions. For similar reasons, there is also a negative but weaker east-west gradient for PBLH at 12 UTC, with slightly lower PBLH in the western United States (Figure 7b), and hours of maximum and minimum PBLH are generally earlier in the east than the west (Figures 7c and 7d).

At the diurnal scale, hours of maximum PBLH are after 20 UTC over most of CONUS, including after 22 UTC over the west and south of the Rocky Mountains. Hours of maximum PBLH derived from AMDAR and ERA5 data agree well, except for several airports in the coastal and eastern regions (Figure 7c).
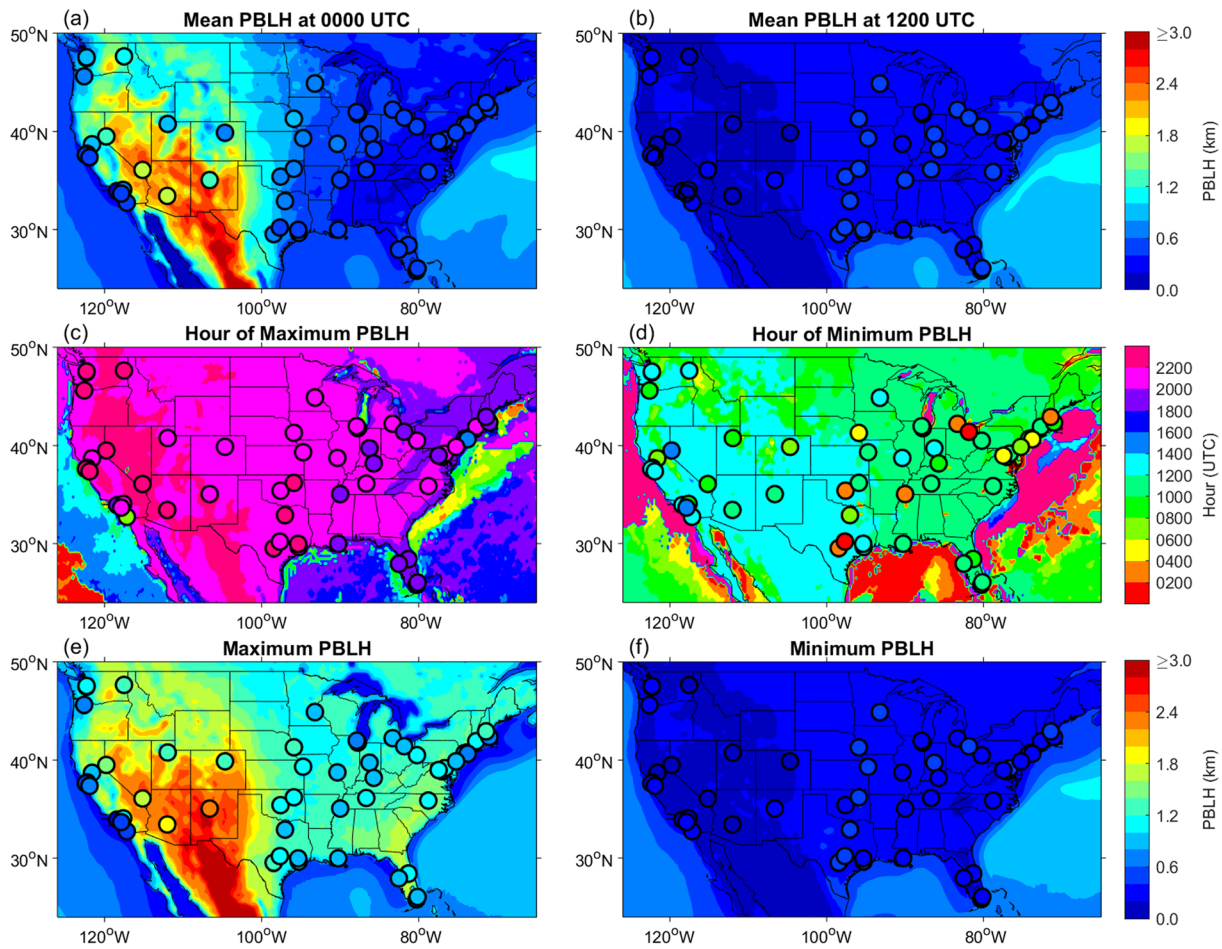
Figure 7. Spatial distributions of mean PBLH at (a) 00 UTC and (b) 12 UTC, hours of (c) maximum and (d) minimum PBLH in the diurnal cycle, and (e) maximum and (f) minimum PBLHs over CONUS in spring from AMDAR (dot symbols) and ERA5 data (background color).

However, hours of minimum PBLH derived from AMDAR and ERA5 data show considerable differences, especially at airports along the northeast coast and the Great Plains (Figure 7d). This may be caused by two reasons. First, unambiguously identifying the PBLH for stable boundary layers remains a challenge (Seibert, 2000). Second, the amount of AMDAR samples from midnight to early morning, when the hour of minimum PBLH usually occurs, is much less as shown in Figure 5b. The small number of samples can lead to large uncertainties in the identified hour of minimum PBLH.

The diurnal maximum and minimum PBLHs are illustrated in Figures 7e and 7f, respectively. There is also an overall east-west gradient for the maximum PBLH demonstrated by both AMDAR and ERA5 data, with the largest value over 2 km in the Southwest. According to the regional categorization in Findell and Eltahir (2003), the regions with higher PBLH coincide with the high-elevation arid areas. The less latent and more sensible heat flux at the surface in drier areas and the larger surface roughness in high mountain areas should contribute to the higher PBLH (Liu & Liang, 2010; Seidel et al., 2012). The minimum PBLH is typically less than 0.5 km over most of CONUS, with slightly lower values in the western regions (Figure 7f). The lower PBLH in the western regions could be also associated with the dry soil and high elevation, both of which favor stronger surface radiative cooling at night. Comparison between the maximum and minimum PBLH indicates that the diurnal amplitude of PBLH is stronger in the western CONUS.

In summer, the east-west gradient for PBLH at 00 UTC becomes stronger than that in spring, with PBLH larger than 2 km over most of the western part while less than 0.5 km over the eastern part (Figure 8a). Although the overall patterns for hours of maximum and minimum PBLH are similar to those in spring,
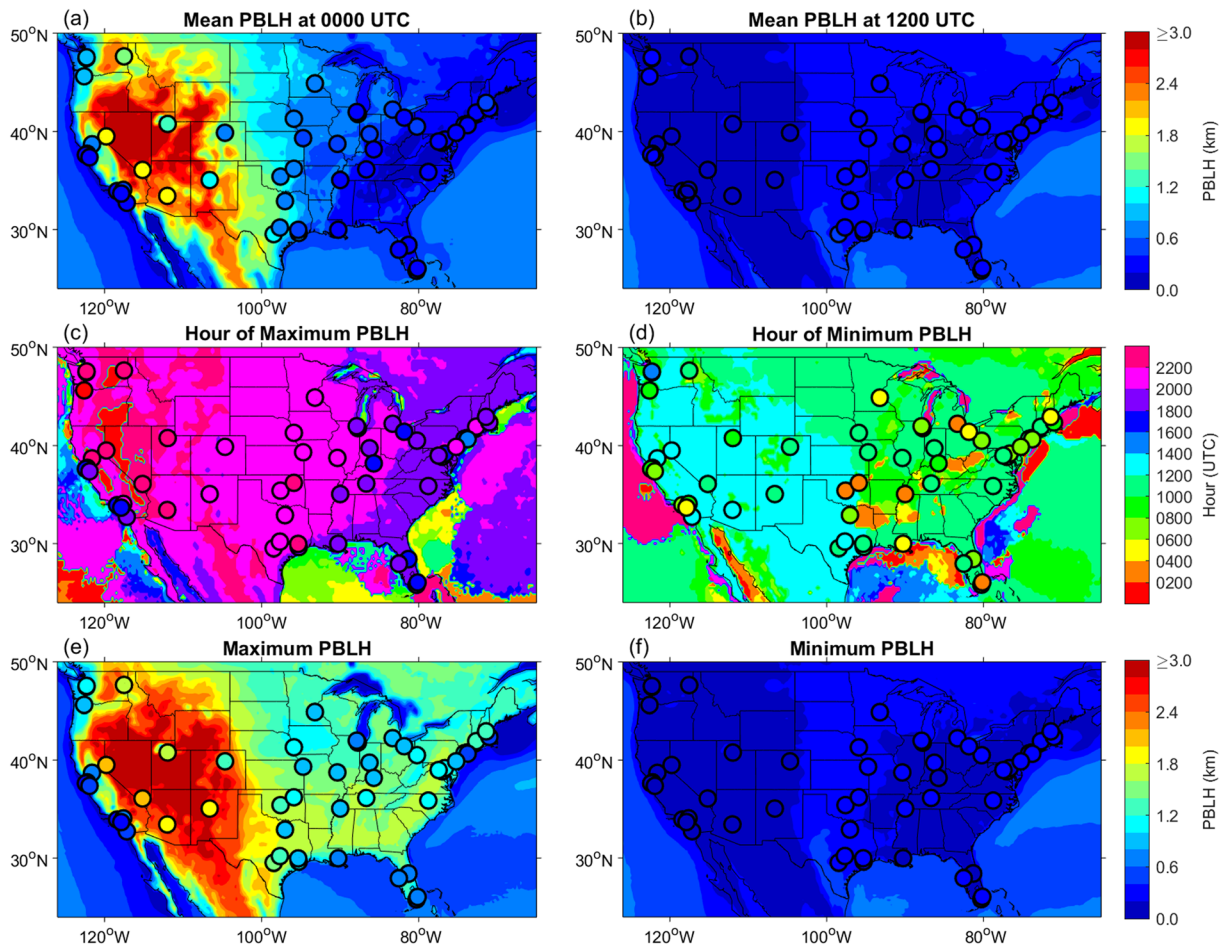
Figure 8. Similar to Figure 7, but in summer.

the maximum PBLH appears earlier at 18–20 UTC over the eastern coastal areas (Figure 8c), which is likely associated with the earlier sunrise in summer. Compared with results in spring, the maximum PBLHs from both AMDAR and ERA5 data generally increase in summer. In particular, the zone with maximum PBLH larger than 2 km extends from the southwest to the northwest (Figure 8e).

The mean PBLH at 00 UTC follows a significantly downward trend from summer to autumn and then winter over the western United States (Figures 9a and 10a). Concomitantly, the east-west gradient of PBLH gradually reduces and virtually disappears in winter. The mean PBLH at 00 UTC is less than 0.5 km over most of the CONUS in winter (Figure 10a). From summer to winter, there is no significant change in hours of maximum PBLH, while the minimum PBLH appears gradually later over most of the CONUS (compare Figures 9c, 9d, 10c, and 10d with Figures 8c and 8d), which could be associated with the persistently delayed sunrise. Compared to its counterpart in spring and summer, the maximum PBLH decreases over the CONUS in autumn and winter, indicated by both AMDAR and ERA5 data (Figures 9e and 10e). In addition, there is a visible north-south gradient for maximum PBLH over the CONUS in autumn and winter, especially in the ERA5 data. It implies that the sun angle, higher in the lower latitude, plays a key role in modulating the spatial distribution of the maximum PBLH in autumn and winter.

When comparing the PBLH patterns in the four seasons, the PBLH at 00 UTC has a marked seasonal variation over the western CONUS but is nearly invariant over most parts of the eastern CONUS. The PBLH at 12 UTC has no significant seasonal variation over the CONUS. The maximum PBLH shows seasonal variations over most parts of CONUS, while the minimum PBLH has no significant seasonal variation, implying that the diurnal amplitude of PBLH would exhibit significant seasonal variations. By comparing the 00 and 12
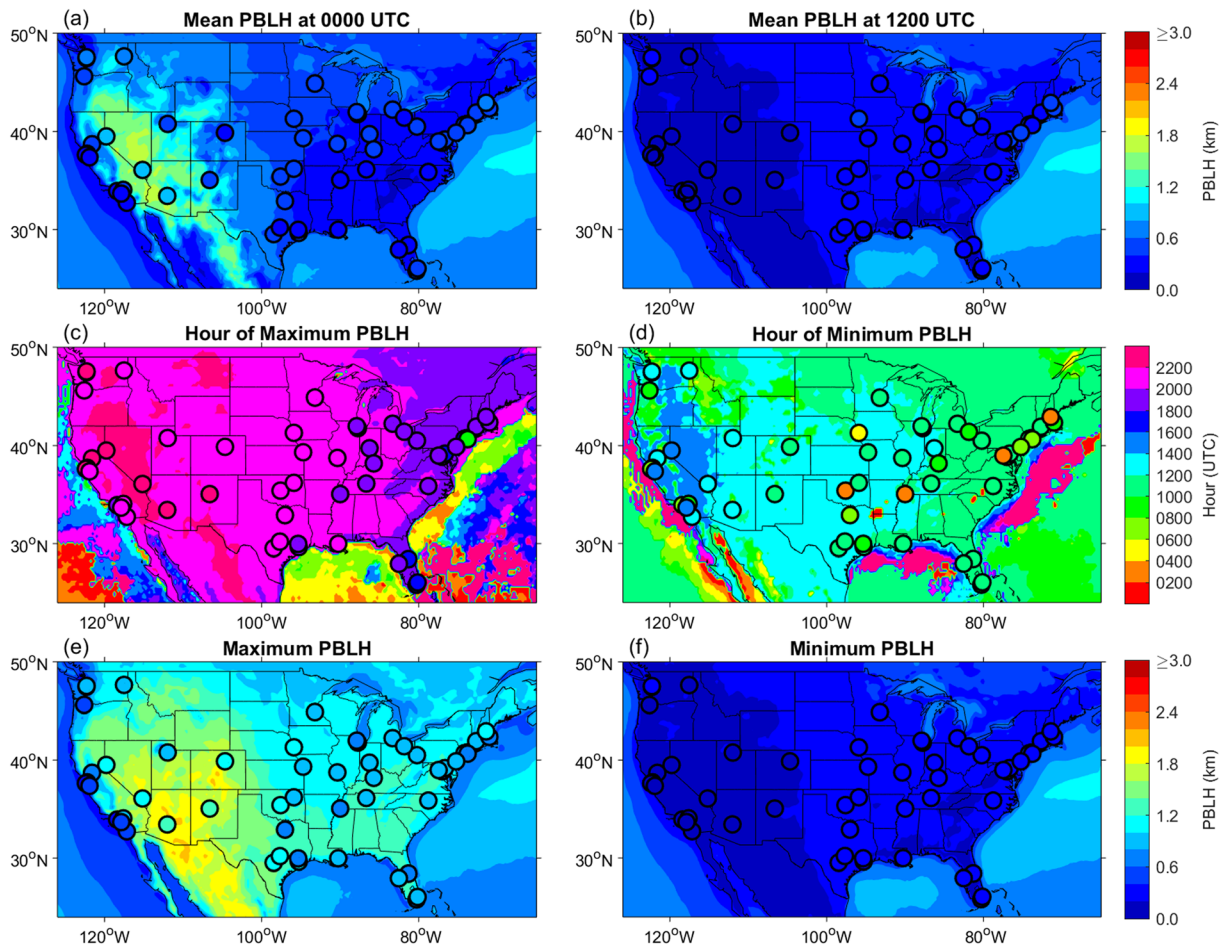
Figure 9. Similar to Figure 7, but in autumn.

UTC PBLH to the maximum and minimum PBLH, we find that the traditional twice-daily radiosonde observations at those two times may roughly capture the diurnal amplitude of PBLH over the western CONUS but not the eastern CONUS. The ERA5 data show overestimations for the maximum PBLH at most airports, but good agreement for the minimum PBLH. Thus, the ERA5 data are also expected to show stronger diurnal variations of PBLH when compared with AMDAR data, which will be examined in the following subsections.

4.3. Comparison Between Spatially Averaged AMDAR and ERA5 PBLH Diurnal Profiles

To comprehensively evaluate the ERA5 PBLH, comparisons between the AMDAR PBLH and the ERA5 PBLH are further conducted in terms of spatially averaged diurnal cycles and scatterplots of seasonal mean values at each hour over all airports (Figure 11). The ERA5 PBLHs are spatiotemporally sampled at AMDAR observation times and the nearest grid cells to the AMDAR airports. The mean ERA5 PBLHs at four nearest grid cells around the AMDAR airports are also used in the comparison between AMDAR and ERA5, which showed similar results (not shown). To make the hourly diurnal profiles comparable and easily interpretable, the PBLHs are presented in LST. In all seasons, the ERA5 PBLH shows significant overestimations during daytime while good agreement with AMDAR at nighttime. The daytime overestimation of ERA5 PBLH is most prominent in the afternoon hours, during which the maximum PBLH typically occurs. However, there is good agreement between AMDAR and ERA5 PBLH during the morning and evening transitions (around 06 and 19 LST, respectively), which is consistent with the results reported by Seidel et al. (2012) who compared PBLHs from radiosonde soundings and ERA-Interim data at 00 and 12 UTC. Overall, the ERA5 PBLH can capture the diurnal phase well but is subject to significant overestimations in the
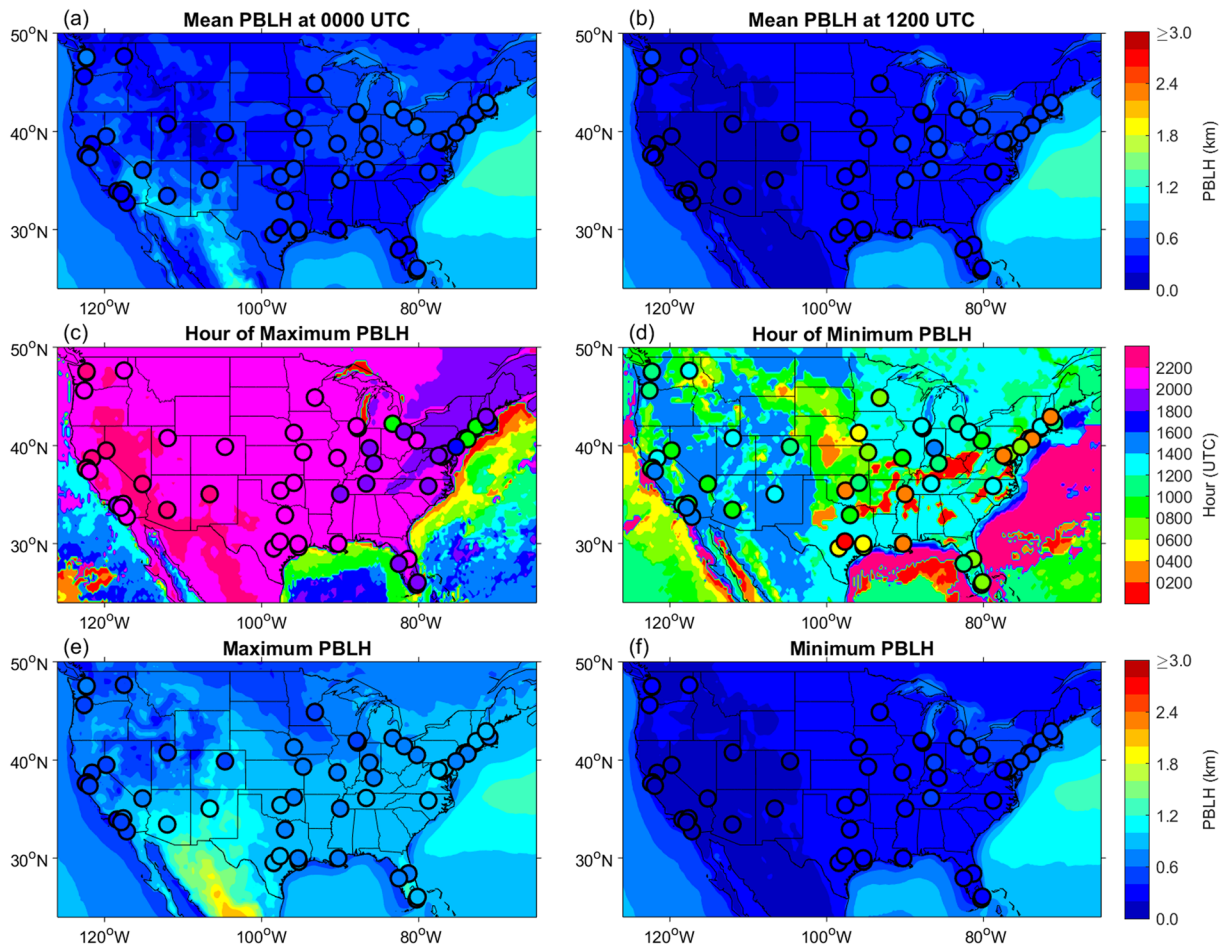
Figure 10. Similar to Figure 7, but in winter.

daytime. The spatial variabilities of the ERA5 PBLH (shown as the shades in top panels of Figure 11) are also larger than those of AMDAR PBLH during daytime.

The scatterplots in the bottom panels of Figure 11 further verify the results discussed above. The PBLHs in the afternoon hours indicated by cyan and blue colors are mostly above the 1:1 line, implying a general over-estimation by ERA5 in all seasons. The PBLHs in the early morning and late evening hours, indicated by red and magenta colors, respectively, show relatively good agreement between AMDAR and ERA5, although there is occasional underestimation by ERA5. These results suggest that it is important to consider the biases in the ERA5 PBLH when using it for PBL studies and air quality applications. The correlation coefficients demonstrate that these two PBLH data sets are highly correlated (correlation coefficient ~0.9), which makes it possible to conduct simple linear bias correction on the ERA5 PBLH based on the AMDAR PBLH.

It should be pointed out that the ERA5 PBLH is estimated by the Ri_b method but with $Ri_{bc} = 0.25$ and $b = 0$, following Seidel et al. (2012). As a result, the differences between the AMDAR and ERA5 PBLH could be partly caused by the differences in terms of the parameters used in the Ri_b method. To quantify whether the overestimations of PBLH by ERA5 data are simply due to such differences in the parameters, the ERA5 PBLH is also compared to the AMDAR PBLH estimated with the same parameters (Figure S11). The new results show even larger biases during daytime and opposite biases at nighttime relative to those presented in Figure 11, which is consistent with our sensitivity test in section 3.2, which shows that the PBLHs calculated using $Ri_{bc} = 0.25$ and $b = 0$ are generally lower than those using $Ri_{bc} = 0.5$ and $b = 100$ (see Figure 3). This implies that the biases in the ERA5 PBLH in Figure 11 cannot be explained by the differences in the parameter setting. To quantify the biases in ERA5 PBLH, we compare AMDAR with PBLH
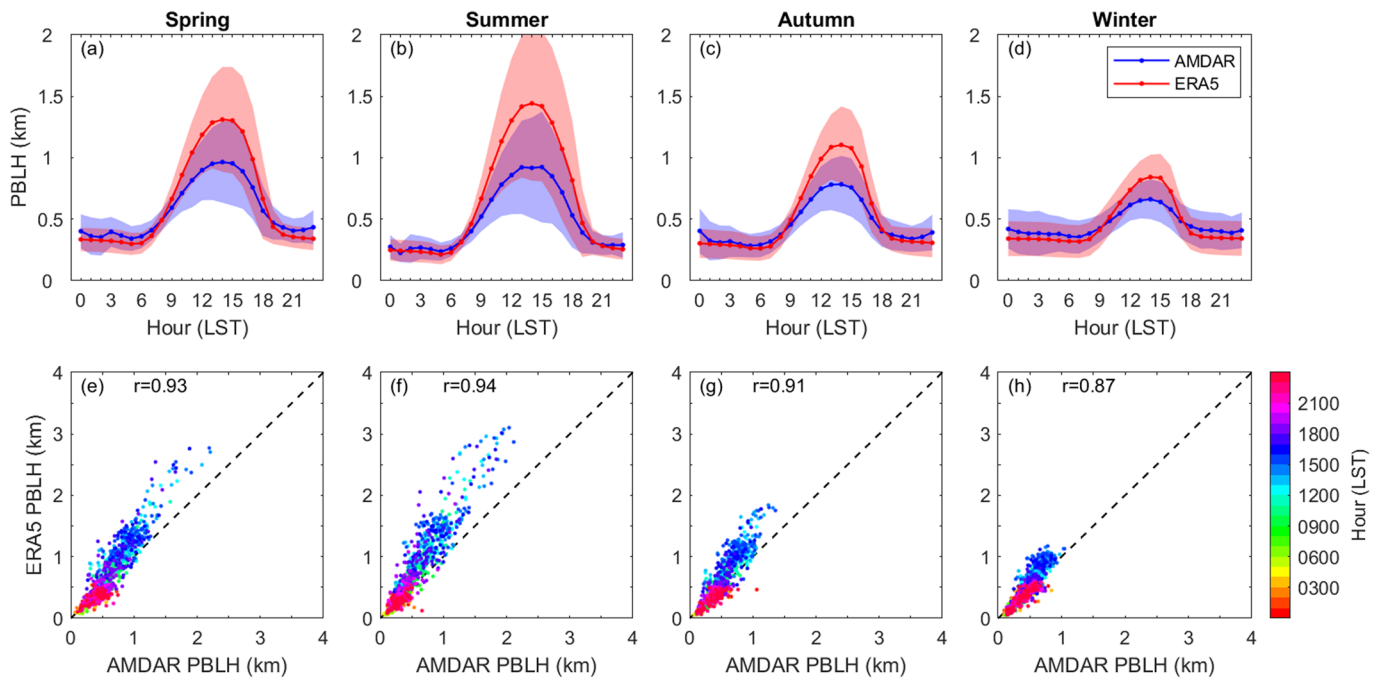
Figure 11. (top panels) Diurnal variations of mean PBLHs from AMDAR (blue solid lines) and ERA5 data (red solid lines) in each season. The results are averaged over 2007–2016 and over 54 airports. The blue and red shades indicate the standard deviations of AMDAR and ERA5 PBLHs, respectively. (bottom panels) Scatterplot comparing the seasonal mean PBLHs from AMDAR and ERA5 data over 54 airports. The local time is shown by the color of dots. The associated correlation coefficients are shown in the top of each panel, which are all statistically significant ($p < 0.05$).

directly provided by ERA5, instead of deriving from ERA5 profiles using exactly the same parameter setting. We also investigate the AMDAR PBLHs estimated using the parameter set of $Ri_{bc} = 0.5$, $u_* = 0.3$ m/s ($b = 100$), and $z_s = 40$ m (Figure S12), which show similar geographic variability as shown in Figures 7–10 but overall larger values across the diurnal cycles compared to results in Figure 11. Both of these sensitivity tests imply that the surface friction term is important in the PBLH computation with the Ri_b method.

4.4. Geographic Variability of the Difference Between ERA5 and AMDAR PBLH Diurnal Profiles

As discussed in section 4.2, the PBLH diurnal climatology exhibits strong geographic variabilities. In order to explore the performance of ERA5 PBLH over different regions, Figure 12 presents the spatial distribution of PBLH diurnal variation amplitude (the middle panel) and the spatially averaged PBLH diurnal cycles over different regions. The results shown here are annual averages over 2007–2016, with seasonal averages presented in Figures S13–S16. Regions 1–8 are divided according to the similarity of PBLH diurnal amplitude (indicated by the color of dots in the middle panel of Figure 12) and the geography regions, which roughly represent, in order, North Pacific, Intermountain West, South Pacific, Central West, South, Central North, Northeast (parts of New England and Middle Atlantic), and Southeast (Florida).

Both AMDAR and ERA5 capture the spatial variability of PBLH diurnal cycle across different regions. The strongest PBLH diurnal cycle occurs in mountainous areas (Region 2). The PBLHs during the afternoon hours are over 1.0 km, much higher than those in other regions, while the nighttime PBLHs are around 0.25 km, significantly lower than those in other regions except South Pacific (Region 3). The stronger diurnal variation with higher daytime PBLH and lower nighttime PBLH in mountainous areas is largely associated with the dry soil conditions and high elevation (Santanello et al., 2018), as discussed in section 4.2. A recent study (Guo et al., 2019) also suggested that the PBLH estimated from radiosonde data is negatively correlated with soil moisture at long time scales.

In contrast, the PBLH diurnal variation is the weakest in the South Pacific area (Region 3), with lower PBLH throughout the diurnal cycle compared to other regions. PBLHs in most hours are less than 0.5 km, with a minor peak around 13 LST. Most airports in this region are located in the coastal area with the diurnal
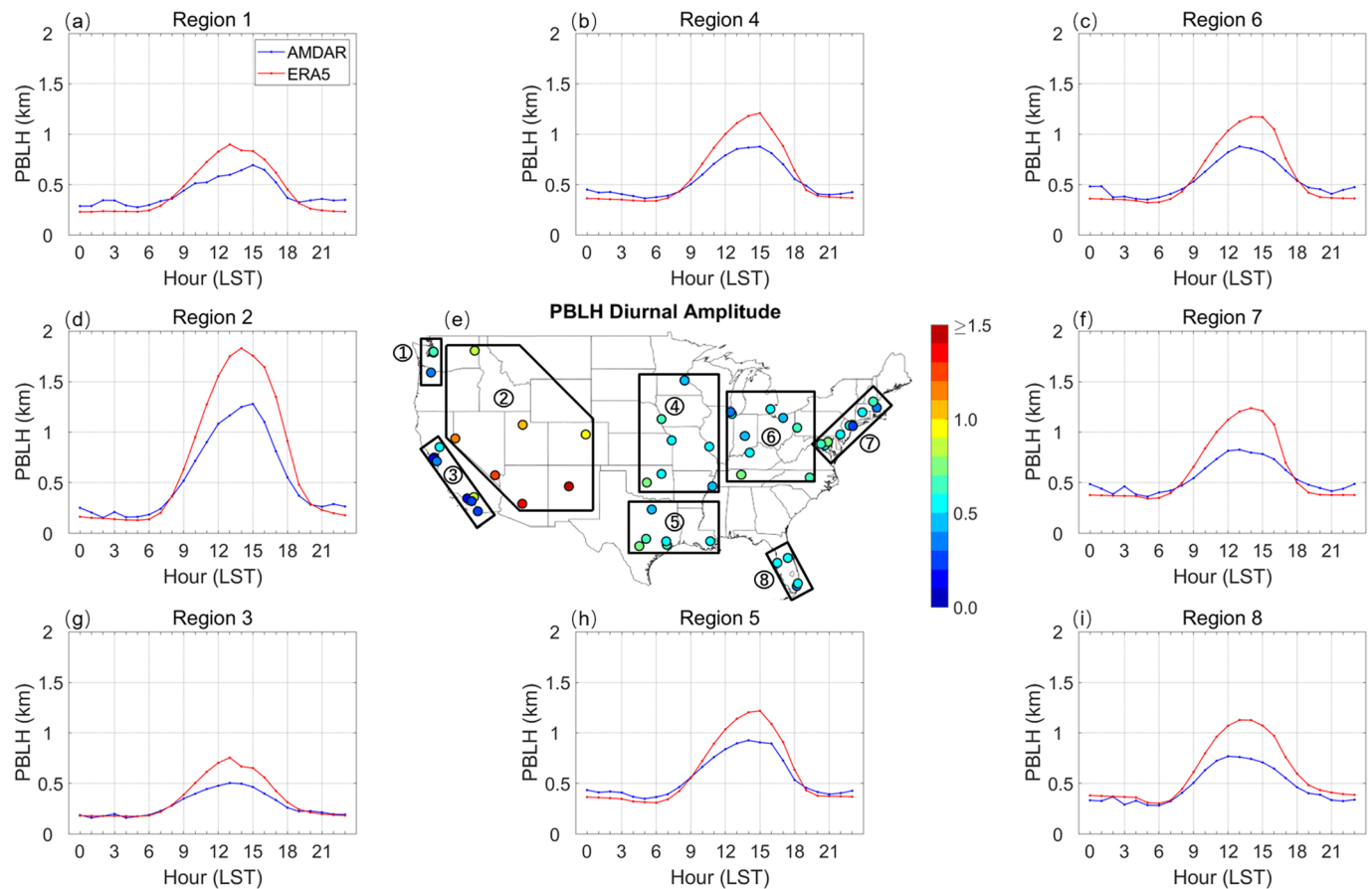
Figure 12. Diurnal amplitude (maximum minus minimum, unit is km) of PBLH based on AMDAR data at 54 airports (middle panel), and the spatially averaged diurnal cycles of PBLH over eight regions (surrounding panels). The results are annual averages over the period 2007–2016.

amplitude of PBLH less than 0.5 km (the middle panel in Figure 12). These PBLH characteristics are likely influenced by the marine environment, since most of the aircraft observations at coastal airports were taken over the ocean due to noise-abatement policies. The weak PBLH diurnal cycle is thus largely due to the small diurnal variation of sea surface temperature. Clouds in the marine boundary layer could also play an important role in weakening the diurnal variation of PBLH (e.g., Rahn & Mitchell, 2016; Stevens et al., 2003), as clouds suppress the PBL development during daytime while reduces radiative cooling at nighttime.

In other regions, the PBLH diurnal amplitude is mostly within the range of 0.5–1.0 km (the middle panel in Figure 12), with lower daytime PBLH in coastal areas (Regions 1 and 7–8) than the inland areas (Regions 4–6). In addition to the PBLH diurnal amplitude, it is also found that there are regional differences in the PBLH diurnal phase. In the west of Mississippi (including Regions 1–5), the daytime PBLH increases slowly but decreases quickly after reaching the maximum at around 14–15 LST, while in the east (including Regions 6–8), the daytime PBLH increases quickly but decreases slowly, with an earlier peak around 12–13 LST. Note that here the annual averaged PBLH diurnal cycle is shown. The seasonal averaged PBLH diurnal cycle in each zone (Figures S13–S16) is similar to that shown in Figure 11 (top panels), with the exception of Regions 3 and 8 where most airports are located in the coastal areas and the PBLH diurnal cycles have no significant seasonal variations.

It can be seen that the ERA5 PBLHs show general overestimations during daytime in all regions, which is consistent with the spatially aggregated results shown in Figure 11. Table 2 shows the absolute and relative biases of ERA5 PBLHs from AMDAR PBLHs averaged over the daytime and the differences of PBLH peak hours between ERA5 and AMDAR data in different regions. In terms of annual mean, the daytime

Table 2
Absolute and Relative Biases of ERA5 PBLHs Compared to AMDAR PBLHs (ERA5 Minus AMDAR) During the Daytime (From 08 LST to 18 LST) and Differences of PBLH Peak Hours Between ERA5 and AMDAR Data (ERA5 Minus AMDAR) in Each Region in Terms of Annual and Seasonal Mean

		Region 1	Region 2	Region 3	Region 4	Region 5	Region 6	Region 7	Region 8
Absolute bias (m)	Annual	138	388	133	176	151	168	231	240
	Spring	181	430	167	174	110	157	261	276
	Summer	325	760	143	314	313	298	363	272
	Autumn	72	331	133	146	158	135	173	225
	Winter	−28	49	85	57	25	72	125	184
Relative bias (%)	Annual	25	41	31	23	18	21	31	36
	Spring	27	36	31	19	11	18	32	35
	Summer	58	61	37	38	36	37	48	48
	Autumn	13	42	33	19	20	17	23	34
	Winter	−8	4	19	9	2	11	18	28
Peak hour difference (hr)	Annual	−2	−1	0	0	1	1	1	1
	Spring	−2	0	0	0	−1	1	2	−1
	Summer	−2	−1	−1	0	0	1	1	1
	Autumn	−2	0	0	1	1	2	1	1
	Winter	−1	0	0	1	1	1	1	1

absolute biases are larger in Region 2 (Intermountain West) and 7–8 (east coast) with mean values over 200 m. Region 3 (South Pacific) also shows larger relative biases (above 30%). Region 2 (Intermountain West) shows the largest absolute (388 m) and relative (41%) biases. Both the absolute (< 200 m) and relative (~20%) ERA5 PBLH biases are smaller in the central regions (Regions 4–6). In terms of seasonal mean, the daytime absolute and relative biases of ERA5 PBLHs compared to AMDAR PBLHs are the largest in summer while the smallest in winter in all regions. Combining the peak hour differences in Table 2 with the diurnal profiles in Figure 11, here we further observe that the ERA5 data fail to capture the PBLH peak time, showing generally earlier and later hours of maximum PBLH than AMDAR data in western (Regions 1–3) and eastern regions (Regions 6–8), respectively. Furthermore, in Regions 6–8, the daytime ERA5 PBLHs generally increase slowly but decrease quickly, which is contrary to AMDAR PBLHs. In summary, the ERA5 PBLHs show considerable biases in the daytime PBLH amplitude (18–41%) over the whole CONUS, especially in summer (36–61%), and earlier (later) peak time in the western (eastern) regions. The ERA5 PBLH shows relatively better agreement with AMDAR data over the central regions (Regions 4–6).

5. Summary

This study presents a climatology of the PBLH based on the data record of hourly AMDAR profiles from 2007 to 2016 at 54 major airports across the CONUS. Several noteworthy features of the PBLH diurnal cycle have been revealed from the AMDAR profiles given their high temporal resolution. The AMDAR PBLHs are also used to evaluate the PBLHs from ERA5 reanalysis data.

The bulk Richardson number method is used to determine the PBLH from AMDAR profiles considering its applicability over a wide range of stability conditions. The estimated PBLH is found to be sensitive to the value of the critical bulk Richardson number (e.g., 0.25 and 0.5) and whether to consider the surface friction effect or not (i.e., $b = 0$ vs. $b = 100$ in Equation 1), especially under stable and near-neutral conditions. In view of this, we estimate PBLHs at four AMDAR airports (BWI, HOU, DEN, and OKC) using a range of parameter sets and compare the results with nearby field campaign observations (DISCOVER-AQ and ARM-SGP). The higher correlation coefficients with $b = 100$ relative to $b = 0$ demonstrate that the surface friction is necessary in the PBLH computation with the Ri_b method. According to the validation results, the parameter set of $Ri_{bc} = 0.5$, $b = 100$, and $z_s = 40$ m is selected to estimate the PBLH from AMDAR profiles.

The PBLH derived from AMDAR profiles show well-defined diurnal cycles of the PBLH, except over coastal areas where the PBLH features weak diurnal variations. The diurnal variation of PBLH is stronger under clear sky than under cloudy conditions and is larger in spring and summer than in autumn and winter. From spring to winter, the spatial pattern of maximum PBLHs gradually transforms from an overall

east-west gradient to a general north-south gradient over CONUS. The former with deeper boundary layers in the western regions appears to be related to the aridity and topography (Guo et al., 2019; Liu & Liang, 2010; Seidel et al., 2012), while the latter is strongly related to the sun angle. Thus, the diurnal amplitude of PBLH is stronger in the western CONUS, especially in spring and summer. These findings about the diurnal climatology of AMDAR PBLHs are consistent with general understanding of PBL diurnal changes (e.g., Seidel et al., 2012) and provide confidence in the applications of AMDAR data in PBL research.

Contrasting the 00 and 12 UTC PBLH to the maximum and minimum PBLH suggests that the traditional twice-daily radiosonde data at these two times may roughly capture the diurnal amplitude of PBLH only over the western CONUS. Previous studies (Seidel et al., 2012) showed good agreement between PBLHs from radiosonde data and ERA-Interim at 00 and 12 UTC. However, our full diurnal comparison between AMDAR and ERA5 reveals consistent overestimation of ERA5 PBLH during the daytime, ranging from 18% to 41% in different regions, which are large in summer and small in winter, while good agreement at night. The ERA5 also fails to capture the peak time of PBLH by 1–2 hr (earlier in western regions but later in eastern regions). Although the AMDAR data are only available at major airports, the tight correlation between AMDAR and ERA5 PBLHs (correlation coefficient ~0.9) implies that it is possible to apply simple bias correction to the ERA5 PBLH in the future, which will lead to a spatiotemporally complete PBLH data set for meteorology and air quality applications. Lastly, we highlight that although the AMDAR data have been extensively validated with collocated radiosonde data in our previous work (Zhang et al., 2019) and many other studies (see Petersen, 2016, for a review), further investigations on quantifying the influence of urban land on the AMDAR profiles (Barlow et al., 2015; Halios & Barlow, 2018; Kotthaus & Grimmond, 2018a, 2018b) and assessing the AMDAR data with high vertical resolution reference data (e.g., from radar systems; see Drüe et al., 2010, for an example), especially in coastal regions, are strongly recommended.

Data Availability Statement

The AMDAR data are available on the Meteorological Assimilation Data Ingest System web service portal (https://madis-data.cprk.ncep.noaa.gov/madisPublic1/data/archive/). We acknowledge the DISCOVER-AQ science team to make the aircraft observation available online (https://www-air.larc.nasa.gov/missions/discover-aq/discover-aq.html).

References

Angevine, W. M., Eddington, L., Durkee, K., Fairall, C., Bianco, L., & Brioude, J. (2012). Meteorological model evaluation for CalNex 2010. *Monthly Weather Review*, *140*(12), 3885–3906. https://doi.org/10.1175/MWR-D-12-00042.1

Angevine, W. M., White, A. B., & Avery, S. K. (1994). Boundary layer depth and entrainment zone characterization with a boundary layer profiler. *Boundary-Layer Meteorology*, *68*(4), 375–385. https://doi.org/10.1007/BF00706797

Barlow, J. F., Halios, C. H., Lane, S. E., & Wood, C. R. (2015). Observations of urban boundary layer structure during a strong urban heat island event. *Environmental Fluid Mechanics*, *15*(2), 373–398. https://doi.org/10.1007/s10652-014-9335-6

Bianco, L., & Wilczak, J. M. (2002). Convective boundary layer depth: Improved measurement by Doppler radar wind profiler using fuzzy logic methods. *Journal of Atmospheric and Oceanic Technology*, *19*(11), 1745–1758. https://doi.org/10.1175/1520-0426(2002)019%3c1745:CBLDIM%3e2.0.CO;2

Blaskovic, M., Davies, R., & Snider, J. B. (1991). Diurnal variation of marine stratocumulus over San Nicolas Island during July 1987. *Monthly Weather Review*, *119*(6), 1469–1478. https://doi.org/10.1175/1520-0493(1991)119%3c1469:DVOMSO%3e2.0.CO;2

Cardinali, C., Isaksen, L., & Andersson, E. (2003). Use and impact of automated aircraft data in a global 4DVAR data assimilation system. *Monthly Weather Review*, *131*(8), 1865–1877. https://doi.org/10.1175/2569.1

Chahine, M. T., Pagano, T. S., Aumann, H. H., Atlas, R., Barnet, C., Blaisdell, J., et al. (2006). AIRS: Improving weather forecasting and providing new data on greenhouse gases. *Bulletin of the American Meteorological Society*, *87*(7), 911–926. https://doi.org/10.1175/BAMS-87-7-911

Cohen, J. B., & Prinn, R. G. (2011). Development of a fast, urban chemistry metamodel for inclusion in global models. *Atmospheric Chemistry and Physics*, *11*(15), 7629–7656. https://doi.org/10.5194/acp-11-7629-2011

Cohen, J. B., Prinn, R. G., & Wang, C. (2011). The impact of detailed urban-scale processing on the composition, distribution, and radiative forcing of anthropogenic aerosols. *Geophysical Research Letters*, *38*, L10808. https://doi.org/10.1029/2011GL047417

Dai, C., Gao, Z., Wang, Q., & Cheng, G. (2011). Analysis of atmospheric boundary layer height characteristics over the Arctic Ocean using the aircraft and GPS soundings. *Atmospheric and Oceanic Science Letters*, *4*(2), 124–130. https://doi.org/10.1080/16742834.2011.11446916

Darby, L. S. (2005). Cluster analysis of surface winds in Houston, Texas, and the impact of wind patterns on ozone. *Journal of Applied Meteorology*, *44*(12), 1788–1806. https://doi.org/10.1175/JAM2320.1

Drüe, C., Hauf, T., & Hoff, A. (2010). Comparison of boundary-layer profiles and layer detection by AMDAR and WTR/RASS at Frankfurt airport. *Boundary-Layer Meteorology*, *135*(3), 407–432. https://doi.org/10.1007/s10546-010-9485-0

ECMWF (2017). Part IV: Physical processes, In *IFS documentation CY43R3* (pp. 1–221). Reading, England: European Centre for Medium-Range Weather Forecasts. Retrieved from https://www.ecmwf.int/node/17736

Eresmaa, N., Karppinen, A., Joffre, S. M., Rasanen, J., & Talvitie, H. (2006). Mixing height determination by ceilometer. *Atmospheric Chemistry and Physics*, *6*(6), 1485–1493. https://doi.org/10.5194/acp-6-1485-2006

Findell, K. L., & Eltahir, E. A. B. (2003). Atmospheric controls on soil moisture-boundary layer interactions. Part II: Feedbacks within the continental United States. *Journal of Hydrometeorology*, *4*, 570–583. https://doi.org/10.1175/1525-7541(2003)004%3c0570:ACOSML%3e2.0.CO;2

Garratt, J. R. (1992). *The atmospheric boundary layer. Cambridge atmospheric and space science series* (p. 335). Cambridge University Press.

Guo, J., Li, Y., Cohen, J. B., Li, J., Chen, D., Xu, H., et al. (2019). Shift in the temporal trend of boundary layer height in China using long-term (1979–2016) radiosonde data. *Geophysical Research Letters*, *46*, 6080–6089. https://doi.org/10.1029/2019GL082666

Guo, J., Miao, Y., Zhang, Y., Liu, H., Li, Z., Zhang, W., et al. (2016). The climatology of planetary boundary layer height in China derived from radiosonde and reanalysis data. *Atmospheric Chemistry and Physics*, *16*(20), 13,309–13,319. https://doi.org/10.5194/acp-16-13309-2016

Guo, P., Kuo, Y. H., Sokolovskiy, S. V., & Lenschow, D. H. (2011). Estimating atmospheric boundary layer depth using COSMIC radio occultation data. *Journal of the Atmospheric Sciences*, *68*(8), 1703–1713. https://doi.org/10.1175/2011JAS3612.1

Halios, C. H., & Barlow, J. F. (2018). Observations of the morning development of the urban boundary layer over London, UK, taken during the ACTUAL project. *Boundary-Layer Meteorology*, *166*(3), 395–422. https://doi.org/10.1007/s10546-017-0300-z

Hastings, D. A., Dunbar, P. K., Elphingstone, G. M., Bootz, M., Murakami, H., Maruyama, H., et al. (1999). *The global land one-kilometer base elevation (GLOBE) digital elevation model, ver 1.0. eds. 1999* (Vol. 325). Boulder, CO: National Oceanic and Atmospheric Administration, National Geophysical Data Center. Available at http://www.ngdc.noaa.gov/mgg/topo/globe.html

Hennemuth, B., & Lammert, A. (2006). Determination of the atmospheric boundary layer height from radiosonde and lidar backscatter. *Boundary-Layer Meteorology*, *120*(1), 181–200. https://doi.org/10.1007/s10546-005-9035-3

Holtslag, A. A. M., & Boville, B. A. (1993). Local versus nonlocal boundary-layer diffusion in a global climate model. *Journal of Climate*, *6*(10), 1825–1842. https://doi.org/10.1175/1520-0442(1993)006%3c1825:LVNBLD%3e2.0.CO;2

Holzworth, G. C. (1964). Estimates of mean maximum mixing depths in the contiguous United States. *Monthly Weather Review*, *92*(5), 235–242. https://doi.org/10.1175/1520-0493(1964)092%3c0235:EOMMMD%3e2.3.CO;2

Hong, S. Y. (2010). A new stable boundary-layer mixing scheme and its impact on the simulated East Asian summer monsoon. *Quarterly Journal of the Royal Meteorological Society*, *136*(651), 1481–1496. https://doi.org/10.1002/qj.665

Jordan, N. S., Hoff, R. M., & Bacmeister, J. T. (2010). Validation of Goddard Earth Observing System-version 5 MERRA planetary boundary layer heights using CALIPSO. *Journal of Geophysical Research*, *115*, D24218. https://doi.org/10.1029/2009JD013777

Konor, C. S., Boezio, G. C., Mechoso, C. R., & Arakawa, A. (2009). Parameterization of PBL processes in an atmospheric general circulation model: Description and preliminary assessment. *Monthly Weather Review*, *137*(3), 1061–1082. https://doi.org/10.1175/2008MWR2464.1

Kotthaus, S., & Grimmond, C. S. B. (2018a). Atmospheric boundary layer characteristics from ceilometer measurements part 2: Application to London's urban boundary layer. *Quarterly Journal of the Royal Meteorological Society*, *144*(714), 1511–1524. https://doi.org/10.1002/qj.3298

Kotthaus, S., & Grimmond, C. S. B. (2018b). Atmospheric boundary layer characteristics from ceilometer measurements part 1: A new method to track mixed layer height and classify clouds. *Quarterly Journal of the Royal Meteorological Society*, *144*(714), 1525–1538. https://doi.org/10.1002/qj.3299

Lange, D., Rocadenbosch, F., Tiana-Alsina, J., & Frasier, S. (2015). Atmospheric boundary layer height estimation using a Kalman filter and a frequency-modulated continuous-wave radar. *IEEE Transactions on Geoscience and Remote Sensing*, *53*(6), 3338–3349. https://doi.org/10.1109/tgrs.2014.2374233

Liu, S., & Liang, X.-Z. (2010). Observed diurnal cycle climatology of planetary boundary layer height. *Journal of Climate*, *23*(21), 5790–5809. https://doi.org/10.1175/2010JCLI3552.1

Marsik, F. J., Fischer, K. W., McDonald, T. D., & Samson, P. J. (1995). Comparison of methods for estimating mixing height used during the 1992 Atlanta field intensive. *Journal of Applied Meteorology*, *34*(8), 1802–1814. https://doi.org/10.1175/1520-0450(1995)034%3c1802:COMFEM%3e2.0.CO;2

McGrath-Spangler, E. L., & Denning, A. S. (2012). Estimates of North American summertime planetary boundary layer depths derived from space-borne lidar. *Journal of Geophysical Research*, *117*, D15101. https://doi.org/10.1029/2012JD017615

Medeiros, B., Hall, A., & Stevens, B. (2005). What controls the mean depth of the PBL? *Journal of Climate*, *18*(16), 3157–3172. https://doi.org/10.1175/JCLI3417.1

Moninger, W. R., Mamrosh, R. D., & Pauley, P. M. (2003). Automated meteorological reports from commercial aircraft. *Bulletin of the American Meteorological Society*, *84*(2), 203–216. https://doi.org/10.1175/BAMS-84-2-203

Petersen, R. A. (2016). On the impact and benefits of AMDAR observations in operational forecasting—Part I: A review of the impact of automated aircraft wind and temperature reports. *Bulletin of the American Meteorological Society*, *97*(4), 585–602. https://doi.org/10.1175/BAMS-D-14-00055.1

Petersen, R. A., Cronce, L., Mamrosh, R., Baker, R., & Pauley, P. (2016). On the impact and future benefits of AMDAR observations in operational forecasting: Part II: Water vapor observations. *Bulletin of the American Meteorological Society*, *97*(11), 2117–2133. https://doi.org/10.1175/BAMS-D-14-00211.1

Rahn, D. A., & Mitchell, C. J. (2016). Diurnal climatology of the boundary layer in Southern California using AMDAR temperature and wind profiles. *Journal of Applied Meteorology and Climatology*, *55*(5), 1123–1137. https://doi.org/10.1175/JAMC-D-15-0234.1

Randall, D. A., Abeles, J. A., & Corsetti, T. G. (1985). Seasonal simulations of the planetary boundary layer and boundary layer stratocumulus clouds with a general circulation model. *Journal of the Atmospheric Sciences*, *42*(7), 641–676. https://doi.org/10.1175/1520-0469(1985)042%3c0641:SSOTPB%3e2.0.CO;2

Ratnam, M. V., & Basha, S. G. (2010). A robust method to determine global distribution of atmospheric boundary layer top from COSMIC GPS RO measurements. *Atmospheric Science Letters*, *11*(3), 216–222. https://doi.org/10.1002/asl.277

Santanello, J. A., Dirmeyer, P. A., Ferguson, C. R., Findell, K. L., Tawfik, A. B., Berg, A., et al. (2018). Land-atmosphere interactions: The LoCo perspective. *Bulletin of the American Meteorological Society*, *99*(6), 1253–1272. https://doi.org/10.1175/BAMS-D-17-0001.1

Sawyer, V., & Li, Z. (2013). Detection, variations and intercomparison of the planetary boundary layer depth from radiosonde, lidar and infrared spectrometer. *Atmospheric Environment*, *79*, 518–528. https://doi.org/10.1016/j.atmosenv.2013.07.019

Schwartz, B., & Benjamin, S. G. (1995). A comparison of temperature and wind measurements from ACARS-equipped aircraft and rawinsondes. *Weather and Forecasting*, *10*(3), 528–544. https://doi.org/10.1175/1520-0434(1995)010%3c0528:ACOTAW%3e2.0.CO;2

Seibert, P. (2000). Review and intercomparison of operational methods for the determination of the mixing height. *Atmospheric Environment*, *34*(7), 1001–1027. https://doi.org/10.1016/S1352-2310(99)00349-0

Seidel, D. J., Ao, C. O., & Li, K. (2010). Estimating climatological planetary boundary layer heights from radiosonde observations: Comparison of methods and uncertainty analysis. *Journal of Geophysical Research*, *115*, D16113. https://doi.org/10.1029/2009JD013680

Seidel, D. J., Zhang, Y., Beljaars, A., Golaz, J.-C., Jacobson, A. R., & Medeiros, B. (2012). Climatology of the planetary boundary layer over the continental United States and Europe. *Journal of Geophysical Research*, *117*, D17106. https://doi.org/10.1029/2012JD018143

Stevens, B., Lenschow, D. H., Vali, G., Gerber, H., Bandy, A., Blomquist, B., et al. (2003). Supplement to dynamics and chemistry of marine stratocumulus—DYCOMS-II. *Bulletin of the American Meteorological Society*, *84*(5), 593–593. https://doi.org/10.1175/BAMS-84-5-Stevens

Stull, R. B. (1988). *An introduction to boundary layer meteorology* (p. 666). Dordrecht, Netherlands: Kluwer Acad. https://doi.org/10.1007/978-94-009-3027-8

Su, T., Li, J., Li, C., Xiang, P., Lau, A. K.-H., Guo, J., et al. (2017). An intercomparison of long-term planetary boundary layer heights retrieved from CALIPSO, ground-based lidar, and radiosonde measurements over Hong Kong. *Journal of Geophysical Research: Atmospheres*, *122*, 3929–3943. https://doi.org/10.1002/2016JD025937

Su, T., Li, Z., & Kahn, R. (2018). Relationships between the planetary boundary layer height and surface pollutants derived from lidar observations over China: Regional pattern and influencing factors. *Atmospheric Chemistry and Physics*, *18*(21), 15,921–15,935. https://doi.org/10.5194/acp-18-15921-2018

Tucker, S. C., Senff, C. J., Weickmann, A. M., Brewer, W. A., Banta, R. M., Sandberg, S. P., et al. (2009). Doppler lidar estimation of mixing height using turbulence, shear, and aerosol profiles. *Journal of Atmospheric and Oceanic Technology*, *26*(4), 673–688. https://doi.org/10.1175/2008JTECHA1157.1

van der Kamp, D., & McKendry, I. (2010). Diurnal and seasonal trends in convective mixed layer heights estimated from two years of continuous ceilometer observations in Vancouver BC. *Boundary-Layer Meteorology*, *137*(3), 459–475. https://doi.org/10.1007/s10546-010-9535-7

Vogelezang, D. H. P., & Holtslag, A. A. M. (1996). Evaluation and model impacts of alternative boundary-layer height formulations. *Boundary-Layer Meteorology*, *81*(3-4), 245–269. https://doi.org/10.1007/BF02430331

Zhang, W., Guo, J., Miao, Y., Liu, H., Song, Y., Fang, Z., et al. (2018). On the summertime planetary boundary layer with different thermodynamic stability in China: A radiosonde perspective. *Journal of Climate*, *31*(4), 1451–1465. https://doi.org/10.1175/JCLI-D-17-0231.1

Zhang, W., Guo, J., Miao, Y., Liu, H., Zhang, Y., Li, Z., & Zhai, P. (2016). Planetary boundary layer height from CALIOP compared to radiosonde over China. *Atmospheric Chemistry and Physics*, *16*(15), 9951–9963. https://doi.org/10.5194/acp-16-9951-2016

Zhang, Y., Gao, Z., Li, D., Li, Y., Zhang, N., Zhao, X., & Chen, J. (2014). On the computation of planetary boundary-layer height using the bulk Richardson number method. *Geoscientific Model Development*, *7*(6), 2599–2611. https://doi.org/10.5194/gmd-7-2599-2014

Zhang, Y., Li, D., Lin, Z., Santanello, J. A., & Gao, Z. (2019). Development and evaluation of a long-term data record of planetary boundary layer profiles from aircraft meteorological reports. *Journal of Geophysical Research: Atmospheres*, *124*, 2008–2030. https://doi.org/10.1029/2018JD029529

Zhang, Y., Wang, L., Santanello, J. A., Pan, Z., Gao, Z., & Li, D. (2020). Aircraft observed diurnal variations of the planetary boundary layer under heat waves. *Atmospheric Research*, *235*, 104801. https://doi.org/10.1016/j.atmosres.2019.104801

Zhu, Y., Derber, J. C., Purser, R. J., Ballish, B. A., & Whiting, J. (2015). Variational correction of aircraft temperature Bias in the NCEP's GSI analysis system. *Monthly Weather Review*, *143*(9), 3774–3803. https://doi.org/10.1175/MWR-D-14-00235.1

Zilitinkevich, S., & Baklanov, A. (2002). Calculation of the height of the stable boundary layer in practical applications. *Boundary-Layer Meteorology*, *105*(3), 389–409. https://doi.org/10.1023/A:1020376832738